

# Time-domain dual pulse coherent control with few-cycle strong-field pulses

**Contact** *w.a.bryan@swansea.ac.uk*

**W A Bryan and G. R. A. J. Nemeth**

*Department of Physics, Swansea University, Swansea, SA2 8PP, UK*

**C R Calvert, R B King, J B Greenwood and I D Williams**

*School of Mathematics and Physics, Queen's University Belfast, Belfast BT7 1NN, UK*

**C M Cacho, I C E Turcu and E Springate**

*STFC Rutherford Appleton Laboratory, Harwell Science and Innovation Campus, Didcot, Oxon., OX11 0QX, UK*

**W R Newell**

*Department of Physics and Astronomy, University College London, London WC1E 6BT, UK*

Quantum mechanics describes internal molecular dynamics in terms of the amplitude and phase of vibrational wavepackets, which are coherent superpositions of states and contain all information about the associated populations and phases. In the energy or frequency domain, the quantum beating is observable by resonant photonic processes; in the temporal domain, this interference results in characteristic time-varying motion. Ultrafast laser systems generating near-infrared (NIR) pulses with durations of hundreds of femtoseconds allowed the first observation of such wavepackets [1,2] with significant applications in chemical dynamics, opening up the field of femtochemistry. Vibrational wavepackets have been observed in a range of systems, often initiated by optical pumping with an ultrafast laser pump pulse and observed by fragmenting the molecule with a similar probe or dump pulse. Recent advances have allowed such wavepacket motion to be resolved in individual molecules [3] through the application of single-molecule detection schemes.

A range of coherent control strategies have been demonstrated whereby temporal or spectral shaping is applied to laser pulse to modify the launch or evolution of vibrational wavepacket motion, thus altering internal states of the molecular system under study [4]. Generally, such modifications require optical coupling between states, and complex spectral or temporal shaping is required to populate pre-defined final state [5]

The vibrational periods of the lightest and simplest molecules  $\text{H}_2^+$  and  $\text{D}_2^+$  are 13 and 20 fs respectively. NIR few-cycle pulses are therefore perfectly suited for imaging vibrational wavepackets as a pulse duration shorter than the vibrational period is readily achievable. Using an interferometrically stable pump-probe configuration and reflection focusing tight enough to generate an intensity of the order  $10^{14} \text{ Wcm}^{-2}$  allows ultrafast strong-field imaging of vibrational motion. The wavepacket is generated by tunnel ionization of the neutral molecules [6] projecting the ground state wavefunction in the neutral molecule onto all vibrational states in the molecular ion.

As with coherent control investigations, once it has been established that a vibrational (or indeed rovibrational) wavepacket has been generated and imaged, it is natural to try to modify its evolution. Spectral shaping unavoidably leads to an increase in pulse duration, which defeats the purpose of employing few-cycle pulses. Recent theoretical predictions indicate a strong-field few-cycle pulse applied at the correct time can heavily perturb a bound electron orbital leading to the transfer of vibrational population as the nuclei adjust nonadiabatically to the rapidly-varying electronic environment

[7-9]. This process can be treated as a dynamic Raman or Stark process. In the former, multiphoton coupling between ground and excited states as wavepacket oscillates causes a bond length (hence time) dependent redistribution; the latter is a polarization of the molecular orbital by the dipole force leading to a time-varying distortion of potential surfaces. The nuclear wavepacket then propagates on the modified potential, and the diabaticity of the process causes population transfer. In both cases, changing intensity, wavelength and intensity of control pulse influences population transfer. Experimental evidence for time-dependent manipulation of a vibrational wavepacket has been presented by the authors [10,11] in comparison with a focal volume integrated quasi-classical model (QCM) [12].

To demonstrate the feasibility of more extensive control of the vibrational state of a molecule with strong-field pulses, we now extend the recently published QCM [12] to two control pulses with independent delays. The proposed technique is distinct from traditional coherent control methods as, rather than applying one shaped pulse, we propose that multiple few-cycle impulsive actions on the wavepacket at well-timed intervals can achieve a useful fidelity of final state. This approach has been discussed for solution to the TDSE for unique double control pulse scenario [13], however here we further the state of the art by systematically investigating the control landscape. Such a study is a demonstration of the efficiency of the QCM, as solving the TDSE repeatedly would take a prohibitive long time.

The QCM is readily modified to include an additional control pulse as the ensemble trajectory motion is modelled at each time-step, allowing a control field of arbitrary complexity. As with the single-control case, the QCM is run out to 750 fs in 50 as steps, and returns the photodissociation yield, phase and population matrices and work done as a function of vibrational state. Operating the QCM 20,000 times requires 42 hours on a standard-performance PC (Intel 2.4 GHz Core 2 Duo P8600, 4 GB RAM, Microsoft Windows 7). Scaling to more complex molecules will require an increase in computing power: each populated electronic state will have to be included, and for tri- and polyatomics, the QCM will have to be extended to cover each active degree of freedom. If resonant control pulses are applied, inter-state coupling will have to be introduced and a more complete representation of rovibrational dynamics is necessary. Finally, as discussed earlier, volume integration is clearly necessary. While such modelling is significantly more advanced than the current discussion, the problem is perfectly suited to parallelization methods.

Experimentally, deriving additional control pulses from one ultrafast pulse is nontrivial as repeated interferometric splitting of the laser output leads to significant losses, leading to a drop in the peak intensities available. An alternative to additional nested interferometers is the use of a focussing optic divided into independently movable annuli, however for large delays, the spatial overlap of the resulting focal volumes would degrade. Furthermore, such optics introduce significant diffraction [14], however the resulting distortion to the pulse wavefronts may compensate for focal walk-off. Another method for introducing independent delays is the azimuthal rotation of glass plates; again, by dividing into annuli, different spatial elements of the pulse can be delayed but this introduces a delay-dependent group-delay dispersion, temporally distorting the pulse. These difficulties could potentially be overcome through the use of a noncollinear geometry, whereby the pump and probe are derived from one interferometer and multiple control pulses from another. While the requirement for tight focusing may make noncollinear propagation difficult, the necessity for the detector to image a restricted section of the focal volume implies that even tight (tens of micron) waists could be overlapped at angles of tens of degrees and still form a common interaction region, and could be improved with diffractive shaping of the foci.

The result of applying dual control pulses (C1 and C2) to the vibrational wavepacket in  $D_2^+$  is presented in figure 1. The delay between the pump ( $t = 0$ ) and probe is scanned for  $0 < (C1, C2) < 200$  fs in 1 fs steps. A pump intensity of  $10^{14}$   $Wcm^{-2}$  is employed to launch the wavepacket and a pump:control intensity ratio of 3:1 is defined for both C1 and C2. To elucidate the transfer of population, the most populated vibrational state as a function of C1, C2 delay is presented as a colour map in figure 1(a). A regular modulation of the most populated state is predicted: at small temporal separations from  $t = 0$ , vibrational states up to  $v = 9$  are populated with a periodicity defined by the average period of oscillation of the  $D_2^+$  molecular ion. At larger delays at constant C1 or C2 delay, an overlap of the repetitive structure is found, the result of the control pulses acting on a more spatially dispersed wavepacket. This effect is magnified along the  $C1 = C2$  diagonal, resulting in a suppressed level of control.

Clearly, the purity of the vibrational population is of interest to coherent control applications and the most populated state is only part of the story, hence the contrast of the population as a function of C1 and C2 is presented in figure 1(b). The contrast is calculated by taking the difference of the peak population to the average of other populations and calculating the ratio to the total population. Groups of pronounced ridges are found with a similar temporal smearing effect as the C1 and C2 delays are increased from  $t = 0$ . Interestingly, the maximum contrast only degrades by a small amount as the C1 and C2 delays are increased, rather the ridges blur into each other, which is again a result of the wavepacket dispersing spatially.

Taken in isolation, the maximum populated state or contrast plots are of limited use. By overlaying the two results, figure 1(c), the relative purity achieved by the dual-pulse control scheme is revealed. Around  $t = 0$ , a poor control outcome is observed. For C1 or C2 delays up to 100 fs, well isolated islands of optimal control are found, allowing single state access up to  $v = 7$  with significant contrast. These regions offer the best chance of experimentally resolving the wavepacket modification. At C1 or C2 delays above 100 fs, the high contrast islands will be difficult to separate, however as the unperturbed wavepacket is known to revive around 580 fs, further investigation is required. Nonequal intensity control pulses may also allow an interesting mix of final states to be populated.

As demonstrated in the single control pulse theoretical and experimental results [10,11], variation of the laser intensity has

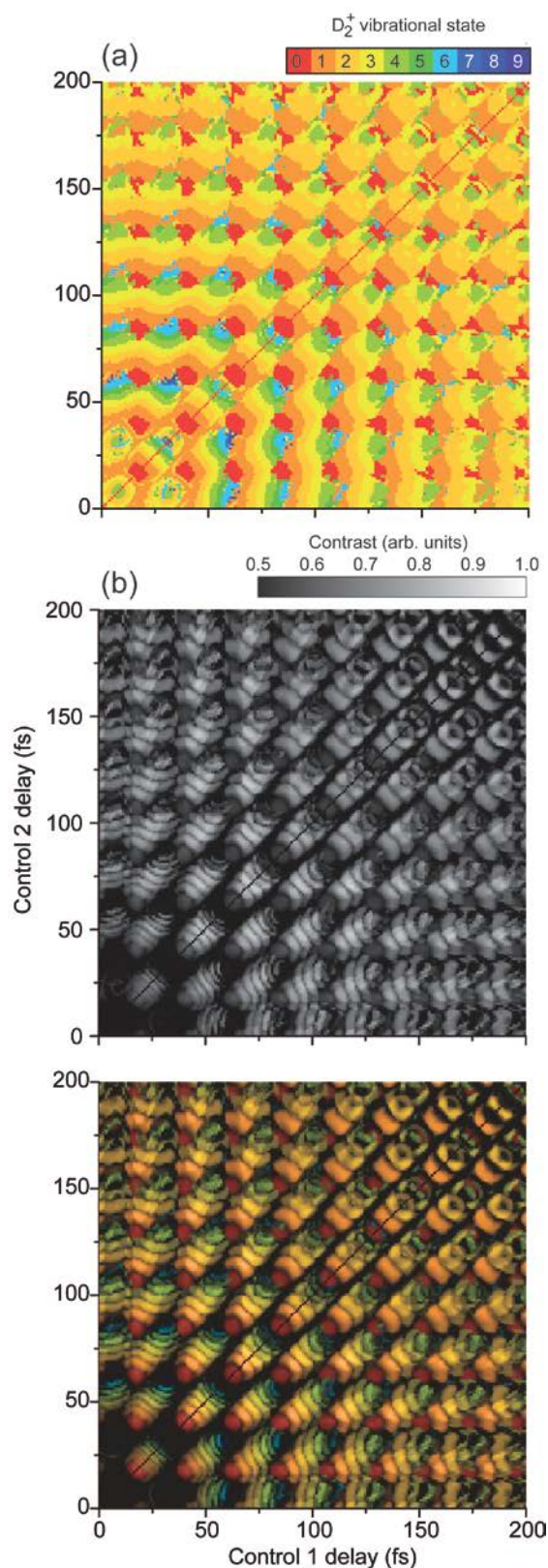


**Figure 1. Modelling the outcome of applying two control pulses to the  $D_2^+$  ensemble. Pump intensity =  $10^{14}$   $Wcm^{-2}$ , pump:control intensity ratio = 3:1, duration of pump, control and probe = 6 fs. (a) Colour map of the most populated vibrational state as control pulses C1 and C2 are scanned from 0 to 200 fs. (b) Vibrational state contrast,  $C$  as a greyscale map, where  $C = (\text{pop}_{\max} - \text{pop}_{\min}) / (\text{pop}_{\max} + \text{pop}_{\min})$ , and  $\text{pop}_{\min}$  is the mean of the remaining populations not equal to  $\text{pop}_{\max}$ . (c) Most populated state and contrast map overlaid to illustrate the final state fidelity that can be achieved, so the ridged colour indicates vibrational state and the luminosity indicates the purity of state.**

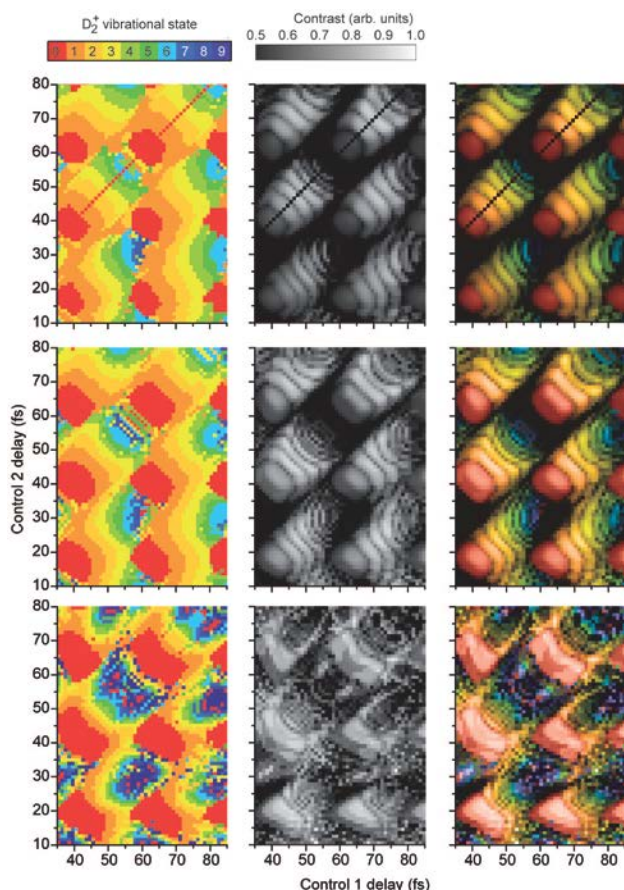


**Figure 2.** Section of the two control pulse landscape as the pump:control ratio is varied from 3:1 (top), 2:1 (middle) and 1:1 (bottom). The pump intensity is  $10^{14}$  Wcm $^{-2}$  and the duration of pump, control and probe = 6 fs. The most populated vibrational state, contrast and final state fidelity as in figure 1.

a dramatic influence on the observability of the control operation. In figure 2, we demonstrate the same is even more so the case for the dual-control pulse scheme. For a fixed pump intensity of  $10^{14}$  Wcm $^{-2}$ , the pump:control intensity is varied from 3:1 (as in figure 1) to 2:1 and 1:1 and a subsection of the C1 - C2 variation landscape is presented where the clearest manipulation is found in figure 1. A pump-control ratio of 2:1 significantly improves the contrast of the final state populations over a ratio of 3:1, particularly for the lowest lying states. This is the result of the more intense control pulse distorting the potential more severely, thus driving all states including the lowest lying. Despite the increase in control intensity from  $3.33 \times 10^{13}$  to  $5 \times 10^{13}$  Wcm $^{-2}$ , the high-contrast maximal population ridges do not shift significantly with C1 or C2 delay.

As the pump:control ratio is further increased to 1:1 the population and contrast of the  $v = 0$  state is observed to be enhanced even further than the 2:1 or 3:1 cases, however the disruption of the ensemble is now so large that all other vibrational states are erratically populated. The loss of the regular structure seen in the 2:1 and 3:1 cases is therefore indicative that the upper useful limit of the dual-control scheme. To further improve the contrast or to populate a pre-defined distribution of states will require additional control pulses.

### Conclusions and outlook

A novel application of the QCM has been presented, allowing a systematic study of the application of two intense few-cycle control pulses. High fidelity population transfer to individual vibrational states is predicted, and following discussions of experimental feasibility, we demonstrate how the range of available states and the transfer contrast depends heavily on the

intensity of the control pulses, establishing an upper limit. With access to more computational power, this systematic approach could be improved to search for an optimal outcome to a pre-defined final state using genetic algorithms, with applications in quantum information.

The manipulation of a vibrational wavepacket by a strong-field control pulse has very interesting applications to attosecond science. It has recently been demonstrated that the localization of the electron in  $D_2^+$  can be externally manipulated by applying a carefully defined light field. By varying the relative phase of the carrier and envelope of a few-cycle pulse (referred to as the carrier-envelope phase, CEP), the electron is observed to be driven from one nuclei to the other. This manipulation of the electron wavepacket is evidenced from the asymmetry of the photodissociation or Coulomb explosion process. Such experimental demonstrations naturally point to controlling the vibrational wavepacket while simultaneously driving the electron motion, theoretically demonstrated by the authors where a significant asymmetry should be observable while modifying the vibrational population. Such methods allowing the nuclear and electronic motions to be selectively directed, allowing additional coherent control routes for strong-field science.

### Acknowledgements

This work was supported by the Engineering and Physical Sciences Research Council (EPSRC) and the Science and Technology Facilities Council (STFC), UK. CRC and RBK acknowledge financial support from the Department of Education and Learning (NI).

### References

1. A. H. Zewail, *Science*, **242**, 1645–1653 (1988)
2. M. J. Rosker, T. S. Rose and A. H. Zewail, *Chem. Phys. Lett.*, **146**, 175–179 (1988)
3. D. Brinks, F. D. Stefani, F. Kulzer, R. Hildner, T. H. Taminiau, Y. Avlasevich, K. M'ullen and N. F. van Hulst, *Nature*, **465**, 905–908 (2010)
4. K. Ohmori, *Annual Review of Physical Chemistry*, **60**, 487–511 (2009)
5. C. Brif, R. Chakrabarti and H. Rabitz, *New J. Phys.* **12**, 075008 (2010).
6. C. R. Calvert, W. A. Bryan, W. R. Newell and I. D. Williams, *Phys. Rep.* **491** 1-28 (2010)
7. H. Niikura *et al*, *Phys. Rev. A* **73** 021402 (2006).
8. D. S. Murphy *et al*, *J. Phys. B* **40** S359 (2007).
9. D. S. Murphy *et al*, *New J. Phys.* **9** 260 (2007).
10. W. A. Bryan *et al*, *Phys. Rev. A* **83**, 021406(R) (2011)
11. W. A. Bryan *et al*, *Faraday Discussions* (accepted). DOI: 10.1039/C1FD00042J (2011)
12. W. A. Bryan *et al*, *New J. Phys.* **12** 073019 (2010).
13. M. Winter, R. Schmidt and U. Thumm, *Phys. Rev. A*, **80**, 031401 (2009).
14. G. R. A. J. Nemeth and W. A. Bryan, *J. Mod. Optics* (accepted). DOI: 10.1080/09500340.2011.583073

# Redistribution of vibrational population with few-cycle strong-field laser pulses

Contact [w.a.bryan@swansea.ac.uk](mailto:w.a.bryan@swansea.ac.uk)

W A Bryan and G. R. A. J. Nemeth

Department of Physics, Swansea University, Swansea, SA2 8PP, UK

C R Calvert, R B King, J D Alexander, J B Greenwood and I D Williams

School of Mathematics and Physics, Queen's University Belfast, Belfast BT7 1NN, UK

C A Froud, C M Cacho, I C E Turcu and E Springate

STFC Rutherford Appleton Laboratory, Harwell Science and Innovation Campus, Didcot, Oxon., OX11 0QX, UK

W R Newell

Department of Physics and Astronomy, University College London, London WC1E 6BT, UK

## Introduction

Advances in ultrafast laser technology now allow the motion of vibrational wavepackets to be imaged through the use of nonresonant strong-field laser pulses with the experiments generally carried out on single electron molecular ions or electronically isolated systems. In particular the hydrogen diatomics provide a crucial test-bed, leading to new discoveries in molecular dynamics and control [1]. In recent years, several substantial developments have been made in this field, owing to the production of few-cycle near-infrared (NIR) laser pulses with durations on sub-vibrational timescales. Such pulses are ideal for manipulation of potential landscapes for steering molecular wavepacket evolution. In recent pioneering studies the ability to control electron localisation during molecular dissociation has been demonstrated in the deuterium molecular ion [2]. Here, the electric field of the laser pulse has been used to couple the electronic states in the molecular ion and guide the electron during the photodissociation (PD) event. Innovative imaging techniques have also been developed through studies in this molecule, where the 'molecular clock' and PACER schemes have availed of electron recollision dynamics. XUV attosecond pump pulses have also been employed to initiate vibrational dynamics, with the authors reporting the necessity to consider the influence of the NIR probe [3,4]. The evolution of nuclear wavepackets in the molecular ion underpin each of these developments, and the ability to manipulate such vibrational dynamics promises to provide a significant step in enhancing molecular control schemes. However, whilst there has been progress in time-resolved imaging (see [1] and references therein), experimental control of the vibrational distribution which dictates wavepacket evolution has remained elusive.

Here, we apply a three-pulse sequence to create, manipulate and probe a vibrational wavepacket and report vibrational redistribution in a bound wavepacket in  $D_2^+$ . Through probing the modified wavepacket, we find systematic trends observed in the experimental results that can be predicted by quasi-classical simulations and hence recover the redistributed vibrational state populations [5]. This is the first observation of such control in this prototypal system. Whilst other multi-pulse studies have demonstrated selective dissociation of a vibrational wavepacket [6], this current work constitutes a more significant breakthrough as the ability to modify the bound vibrational superposition provides a platform for future studies of molecular control (e.g. [7]).

The scheme for wavepacket control is sketched in Fig. 1. The pump pulse initiates tunnel ionization of  $D_2$ , populating a coherent superposition of vibrational states in the electronic ground state ( $1s\sigma_g$ ) of the  $D_2^+$  molecular ion. The manipulation pulse is applied after some delay, during which the vibrational wavepacket has evolved in time, see Fig 1(b-c), and acts to modify the bound wavepacket. Finally, the subsequent evolution of the modified wavepacket is mapped by a probe pulse, via PD of the molecular ion.

The  $D_2^+$  wavepacket created in this scheme is in a broad range of vibrational states, each evolving at a different frequency. The wavepacket initially oscillates across the bound potential surface in a localized form. However due to the anharmonicity of the potential it rapidly undergoes quantum dephasing (shown in Figs 1b and 1c) so that the wavepacket becomes delocalized across the full extent of the potential [1,5,8-11]. The spatial and temporal profile of the vibrational wavepacket is thus inherently dictated by the vibrational population distribution.

Whilst the vibrational distribution is initially set by the pump process, theoretical predictions suggest that the wavepacket can be actually manipulated by an ultrashort laser pulse, leading to modified vibrational state distributions [5,8-11]. It has been noted that some of the most significant redistribution effects occur when the modification pulse is timed to coincide with the initial dephasing of the wavepacket. The experimental approach to this study therefore required three intense laser pulses with variable and interferometrically stable delays. A commercial 30 fs Ti:Sapphire laser with a central wavelength of 790 nm and bandwidth of 35 nm generated 1 mJ pulses at 1 kHz, which were further broadened to 140 nm by self-phase modulation in an argon-filled hollow fibre with a pressure gradient. Following compression by a series of chirped mirrors, the 240  $\mu$ J, 10 fs pulse was split into three pulses with independent delays in a nested Mach-Zehnder interferometer, resulting in 32  $\mu$ J pump, 11  $\mu$ J manipulation and 35  $\mu$ J probe pulses. The synchronization of the three pulses was established using a second-

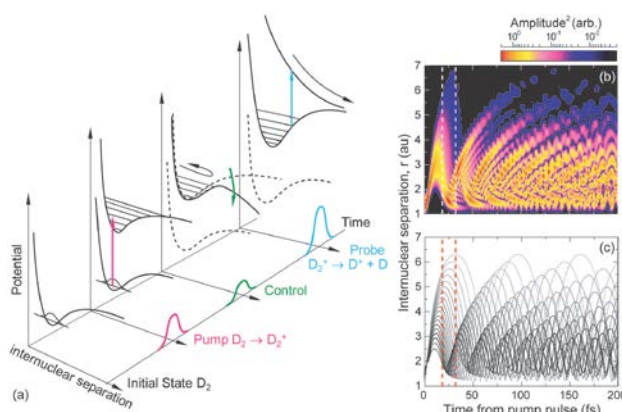


**Figure 1. (a) Schematic of the pump-modify-probe scheme. The pump pulse ( $I = 0.4 - 1.1 \times 10^{14} \text{ Wcm}^{-2}$ ) ionizes  $D_2 \rightarrow D_2^+$  creating a vibrational wavepacket. Following a delay of tens of fs, the modifying pulse ( $I = 1.3 - 3.7 \times 10^{13} \text{ Wcm}^{-2}$ ) distorts the molecular PES. The population redistribution is imaged by photodissociating  $D_2^+ \rightarrow D + D^+$  in the probe ( $I = 0.6 - 2 \times 10^{14} \text{ Wcm}^{-2}$ ). The unperturbed vibrational wavepacket predicted by the time-dependent Schrödinger equation (b) and quasi-classical model (c). The region over which the manipulation pulse is applied is indicated by vertical dashed lines.**

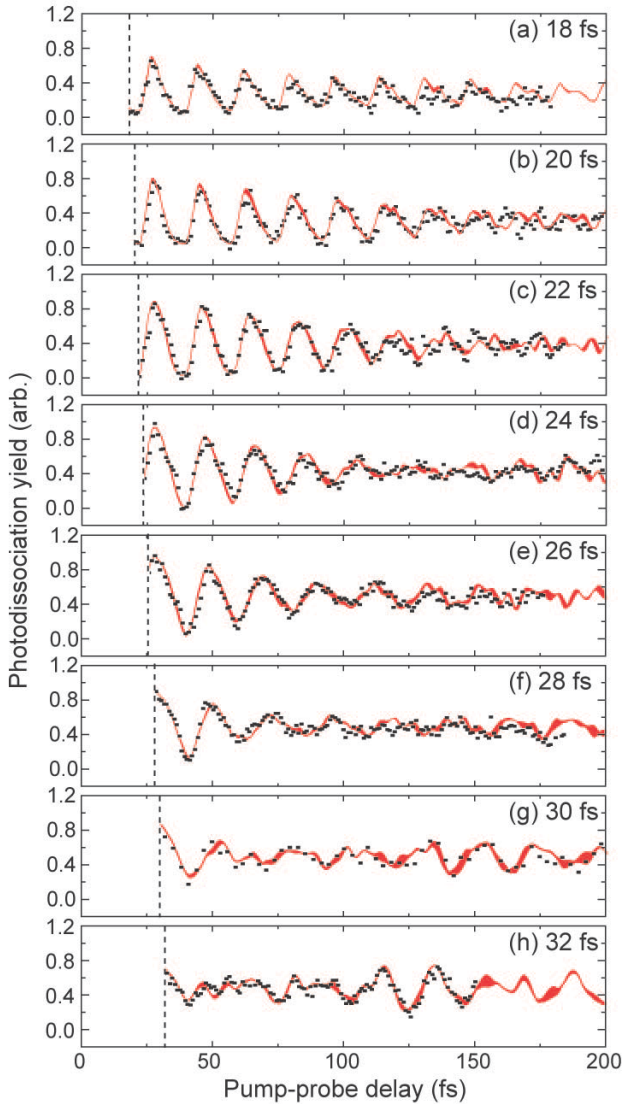


**Figure 2. Experimental PD yield (black dots) for pump-modification pulse delay times from (a) 18 to (h) 32 fs. The corresponding focal-volume-integrated yield is given by the solid red line and the varying vertical thickness indicates the uncertainty in fitting the experimental results**

harmonic autocorrelator containing a 10  $\mu\text{m}$  BBO crystal. The three pulses were combined collinearly and reflection focussed into an effusive jet of room temperature  $\text{D}_2$  in the interaction region of an ion time-of-flight mass spectrometer, used to energetically resolve  $\text{D}^+$  products as a function of delays. The spectrometer contained a 250  $\mu\text{m}$  aperture, hence only the fragmentation of molecules aligned to within a few degrees of the probe polarization direction was observed, essentially reducing this to a 1D problem.

Figs. 2(a) to 2(h) display the experimental PD yield as a function of probe delay for a sequence of discrete manipulation pulse delays ranging from 18 to 32 fs. We have isolated the contribution of the vibrational wavepacket to the PD yield as discussed in [5,12,13]; a bandpass ( $25 < f < 400$  THz) filter is applied, whereby the high frequency cutoff smooths subcycle noise and the low frequency cutoff removes the effects of rotational wavepackets in the neutral molecule. Each set of data describes the behaviour of the modified wavepacket resulting from the effect of the control pulse. As the PD probing event is enhanced near the outer turning point of the  $1\sigma$  potential well, oscillations in the yield serve to map the wavepacket motion. For instance in Fig. 2(a), with the control pulse at 18 fs, it can be deduced that the modified wavepacket evolves in a form that remains well localized as it propagates beyond 150 fs.

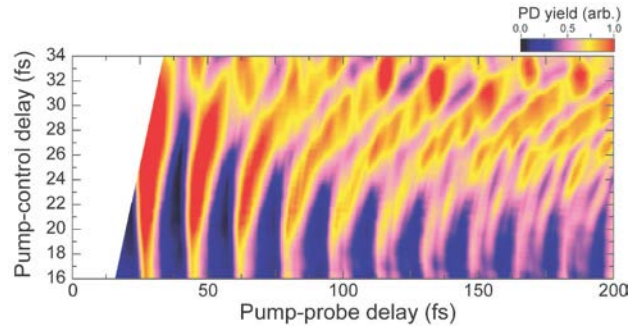


**Figure 3. Predicted PD yield integrated over the focal volume for different pump-manipulation pulse delays between 16 and 34 fs, as a function of pump-probe delay.**

Since the wavepacket is oscillating across the potential, this results in a periodic PD yield with strong signal when the wavepacket is at the outer turning point and weak signal when it is at the inner turning point. On the other hand in Fig. 2(h) it can be observed that delocalization of the wavepacket is an immediate consequence of the application of the manipulation pulse at 32 fs, but with a strong fractional revival seen to occur, centred around 125 fs. Figs. 2(b) to (g) demonstrate a systematic trend between these two extremes. Thus it is immediately apparent that coherent wavepacket motion has been manipulated in this study, with each delay enforcing a different outcome on the subsequent wavepacket evolution.

In order to gain a better understanding of this behaviour, and to characterise the vibrational state redistribution, it is instructive to model the influence of the manipulation pulse. In previous studies we and others have carried out full quantum simulations of such control interactions, taking advantage of the fundamental, effective 2-state nature of the  $\text{D}_2^+$  system. However to compare with the experimental results described here it is necessary to integrate the simulation over the intensity distribution throughout the effective interaction focal volume at each delay. Thus quantum simulations are computationally prohibitive, and instead we have employed a quasi-classical

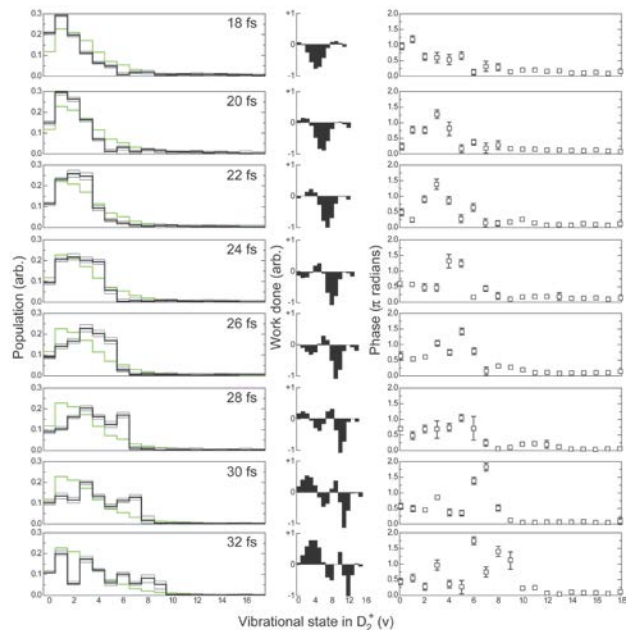


**Figure 4. Simulated vibrational distribution for each manipulation pulse delay. In each plot, the initial distribution created by the pump pulse is given by the light (green) line and modified distribution is the dark (black) line. The uncertainty in population (grey bars) is derived from the uncertainty when fitting the experimental PD yield (Fig. 2).**

model, which has been shown to be consistent with a Schrodinger equation approach in  $D_2^+$  [11] and which has been described in detail elsewhere [5,12] and in pervious CLF Annual Reports.

The PD yields calculated by integrating the quasi-classical model over the range of intensities measured in the experiment for manipulation pulse delays in the range 16 - 34 fs are displayed in Fig. 3. The evolution from a well-localised wavepacket displaying periodic signal at short control delay times, to the more dispersed behaviour as control pulse delay is increased is clearly evident. So too are the 'islands' in the colour map in the 100 - 150 fs range observed at longer control delay times, indicative of partial wavepacket revival.

The results of the simulations have also been displayed as a solid line in Fig. 2, where a fitting procedure has been adopted, with pulse intensities varied in order to obtain a best fit. Sources of uncertainty are defining the zero delay time (estimated as 300 attoseconds from a linear delay calibration), and the range of active intensities (estimated as better than  $8 \times 10^{12}$  Wcm for all three pulses). The agreement in trend with the experimental data (Fig. 2) is strong, indicating that the effect of a manipulation pulse on a bound wavepacket in a practical system can be predictable, even in circumstances where experimental volume effects may be expected to blur the outcome.

Most interesting is that the model also returns corresponding predictions for the redistribution of vibrational state populations. We can thus, through comparison with the experimental PD yield, deduce the modification of the vibrational distribution by the manipulation pulse. These results are shown as black lines in Fig. 4 for the range of control pulse delays employed in the experiment. Also shown as a green line in each case is the initial vibrational distribution as predicted by the ionisation model. It should be noted that this is not a typical Franck-Condon distribution but is instead skewed to lower vibrational states, consistent with other studies of ultrashort pulse ionisation in  $D_2$ .

With a delay around 30 fs between the pump and manipulation pulse, the vibrational population is broadly distributed with meaningful population occurring in up to 10 states. The net effect of this operation is that population from lower states is distributed towards higher vibrational levels. By this time, the initial wavepacket has already executed a full field-free oscillation and is again moving outwards in  $R$ , towards the outer turning point of the potential well. As the potential surface begins to oscillate it acts to accelerate the wavepacket with the net effect of the dynamic Stark interaction imposing a force acting outwards in  $R$  [X]. Thus the population is redistributed with portions moving towards large  $R$  values, i.e. into higher vibrational states.

The converse occurs if the wavepacket is moving inwards in  $R$  when the manipulation pulse is applied. Here the outward force is opposing the motion, decelerating the wavepacket such that the population is redistributed to a subset of lower vibrational levels. This effect is observed for the shorter control delays in Figs. 4(a)-(c), leading to the dominance of fewer states and resulting in the oscillatory wavepacket motion of Figs. 2(a)-(c) where, with fewer states occupied, the wavepacket executes localised motion for a longer period of time prior to any dephasing effects.

## Conclusions

In this letter we have demonstrated that the modification of a bound vibrational wavepacket in  $D_2^+$  by an ultrashort control pulse can be experimentally implemented and quantified. The redistribution of vibrational population can be recovered using a model that incorporates tunnel ionization and dynamic Stark-shift deformation of the potential surface integrated over the focal volume. While this model is approximate, it demonstrates

the validity of applying a strong-field treatments to a simple system. In the future, multiple active electronic orbitals and more than two nuclei will add complexity but may well be theoretically tractable following the reduction to the most significant nuclear co-ordinates. Calculating polyatomic PESs and polarizabilities is well within the capabilities of modern *ab initio* quantum chemistry software, hence predictions for triatomics such as OCS are feasible and could be benchmarked against time-dependent density-functional theory (TD-DFT). Coherent control of complex polyatomic molecules has been demonstrated in the weak ( $< 10^{10}$  Wcm<sup>2</sup>) and intermediate ( $10^{10} < I < 10^{12}$  Wcm<sup>2</sup>) field regimes, see recent reviews for discussions of quantum chemistry, molecular dynamics, wavepacket propagation and optical control of polyatomic systems.

## Acknowledgements

This work was supported by the Engineering and Physical Sciences Research Council (EPSRC) and the Science and Technology Facilities Council (STFC), UK. CRC and RBK acknowledge financial support from the Department of Education and Learning (NI), GRAJN acknowledges financial support from EPSRC and STFC.

## References

1. C. R. Calvert, W. A. Bryan, W. R. Newell and I. D. Williams, *Phys. Rep.* **491** 1-28 (2010)
2. M. F. Kling *et al.* *Science* **312** 246 (2006).
3. M. Kremer *et al.*, *Phys. Rev. Lett* **103** 213003 (2009)
4. G. Sansone *et al.*, *Nature* **465** 763 (2010)
5. W. A. Bryan *et al.*, *Phys. Rev. A* **83**, 021406(R) (2011)
6. F. Kelkensberg *et al.*, *Phys. Rev. Lett.* **103** 123005 (2009).
7. C. R. Calvert *et al.*, *J. Phys. B* **43** 011001 (2010).
8. H. Niikura *et al.*, *Phys. Rev. A* **73** 021402 (2006).
9. D. S. Murphy *et al.*, *J. Phys. B* **40** S359 (2007).
10. D. S. Murphy *et al.*, *New J. Phys.* **9** 260 (2007).
11. T. Niederhausen and U. Thumm, *Phys. Rev. A* **77** 013407 (2008).
12. W. A. Bryan *et al.*, *New J. Phys.* **12** 073019 (2010).
13. W. A. Bryan *et al.*, *Phys. Rev. A* **76** 053402 (2007).

# KEIRA-CHIMERA: a new method in high resolution femtosecond laser mass spectrometry

Contact [mduffy23@qub.ac.uk](mailto:mduffy23@qub.ac.uk) / [j.greenwood@qub.ac.uk](mailto:j.greenwood@qub.ac.uk)

MJ Duffy, O Kelly, L Belshaw, RB King,  
ID Williams, CR Calvert and JB Greenwood

Centre for Plasma Physics,  
School of Mathematics and Physics,  
Queen's University Belfast

## Introduction

The use of electrostatic ion traps as mass spectrometers has been recognised as having great promise [1]. The electrostatic nature of such devices enables the trapping of all ions concurrently as the trapping is independent of mass for ions of the same energy per charge. In a linear Electrostatic Ion Trap (LEIT) ions are trapped along a linear trajectory. It behaves analogous to a laser cavity, with ions oscillating back and forth between the cavity mirrors. The frequency at which an ion oscillates in the cavity is proportional to the square root of its charge-to-mass ratio. Hence by using frequency information extraction techniques a mass spectrum of all trapped ions is produced. This may be done via Fourier analysis of the time spectrum generated by a LEIT; which consists of a series of impulses. We report here details on the KEIRA-CHIMERA technique for high resolution mass spectrometry using a femtosecond laser as an efficient ionization source. This is a novel new technique that combines the power of a linear electrostatic ion trap with a new frequency extraction technique, based on comb-functions, which enables easy generation of a mass spectrum with high resolution from the time spectrum.

## KEIRA

The Kilovolt Electrostatic Ion Reflection Analyser (KEIRA), shown in figure 1, is a LEIT fitted with three pick-up rings used for the non-destructive detection of ions as they oscillate back and forth in the cavity. The pickup rings work on the principle of image charge detection and have been fully calibrated [2] so that ion numbers passing through the pick-up can be calculated.

KEIRA [3] consists of a series of electrodes on which potentials are applied to create an electrostatic mirror and lens pair used to trap ions on a stable linear trajectory in the device. Every time an ion bunch transverses the central field free region they are detected at up to three locations with the pick-up rings. One pick-up ring is placed at the geometric centre of the device. The two off-centre pickups are placed either side of the central pickup. Each pickup generates a time signal that consists of a series of impulses as the ion bunch passes through the pick-up

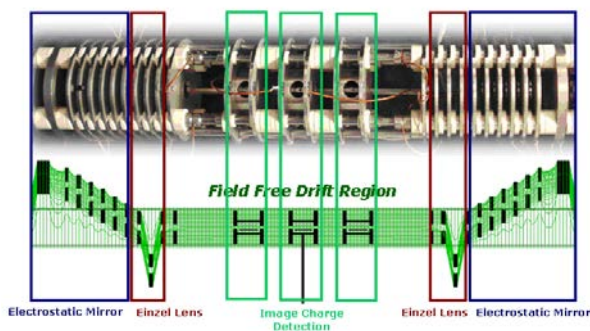


Figure 1 – Top: A picture of the KEIRA device showing the electrodes and locations of the pick-up rings. Bottom: A representation of the potential energy surface generated by the electrodes.

ICE Turco, CM Cacho and E Springate

Central Laser Facility,  
STFC Rutherford Appleton Laboratory,  
Didcot,  
OX11 0QX

on every pass through the device. Ions are generated with a femtosecond laser pulse interacting with a gas target just above one of the end electrodes. This ensures the ion bunches created are well defined in energy and space.

The central pickup data consists of, for a single ion species present in the trap, a series of impulses spaced by half the period of oscillation in the trap. For every ion species present in the trap there will be an additional series of impulses spaced by half that particular ion's period of oscillation. The period of oscillation is proportional to the square root of the mass-to-charge ratio of the ion species.

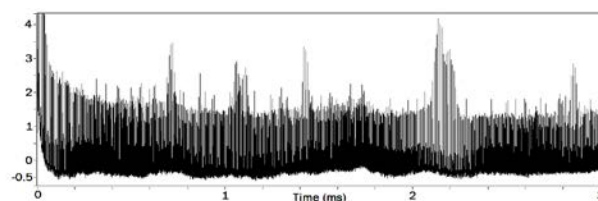


Figure 2 – Example of Xe<sup>+</sup> trapping data. The revivals in signal are when the different Xe isotopes come back into phase with each other.

Figure 2 above shows an example time spectrum of xenon ionised with a femtosecond laser. Xenon is a noble gas with seven different stable isotopes. All the ions created due to the femtosecond laser interaction are initially created at the same point in space and time. As they travel through the trap the different isotopes become spread apart as they have different periods of oscillation. Beating in the spectrum can be seen as time progresses due to different isotopes coming back into phase with each other at the point of detection. There is a rich amount of frequency information contained within each time spectrum

The time domain information can be analysed with Fourier analysis to extract the oscillation frequencies. Due to the non-sinusoidal nature of this data a Fourier transform generates a large number of harmonics. Through use of these higher harmonics high resolution mass information [3] can be extracted for the ion species present in the trap.

However the extraction of a mass spectrum for all ions in the trap is complicated, due to these harmonics. This is because each ion species will have its own unique series of harmonics. Thus even when there are relatively few ion species present, the complexity of the frequency data means that direct conversion to a mass spectrum is non-trivial. In order to circumvent this complication we have developed a new technique, which generates high resolution mass spectrum from the time spectrum information created from KEIRA.

## CHIMERA

The CHIMERA technique (Comb-sampling for High-resolution Impulsetrain frequency ExtRAction) is an advanced algorithm that extracts frequency information from the time spectrum information generated from KEIRA. The extracted frequency spectrum is absent of the harmonics generated from Fourier

analysis but retains the high resolution of the highest harmonics. Thus a mass spectrum of high mass resolution is readily produced.

The CHIMERA algorithm [4] uses a series of test comb-functions that are cross-correlated with the trapping data to generate frequency coefficients for the different ion species. A comb-function is a much better match to the time signal than sinusoids; resulting in better frequency resolution compared with the fundamental Fourier frequency. The drawback of this simple approach is that there are also many fractional harmonics generated in the frequency spectrum.

However, this problem can be ameliorated by acquiring data simultaneously with two pickup rings. To demonstrate this frequency spectra generated with CHIMERA, analysis of simulated data ‘acquired’ from a single oscillating ion species from the central (a) and offset (b) pickup rings is shown in Figure 3.

If these spectra are multiplied together and the square root taken, the fractional harmonics are suppressed and a ‘clean’ frequency spectrum with only the fundamental frequencies dominating is produced. The addition of more pick-up rings would act to reduce any remaining fractional harmonics to an even greater degree.

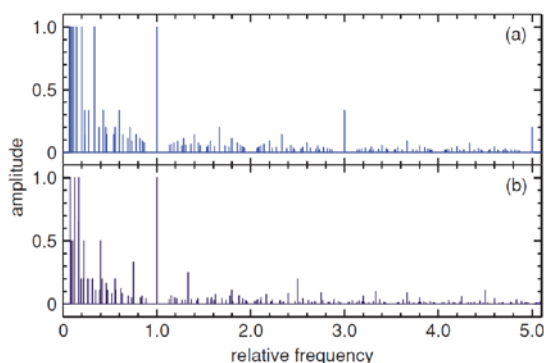


Figure 3 - Frequency spectrum generated from artificial time spectra for (a) central and (b) pick up ring. Note both have a strong contribution at the fundamental but that the fractional harmonics are different.

### Experimental results

Analysis of the data in figure 2 using the CHIMERA algorithm compared to a Fast Fourier Transform (FFT) is shown in figure 4. Both techniques are able to extract the seven fundamental frequencies representing the different isotopes of xenon. The CHIMERA frequency resolution is far superior compared to the fundamental FFT frequency and equivalent to the highest FFT harmonics, but with superior signal to noise ratio. As CHIMERA extracts a single frequency for each isotope it therefore can be readily converted into a mass spectrum.

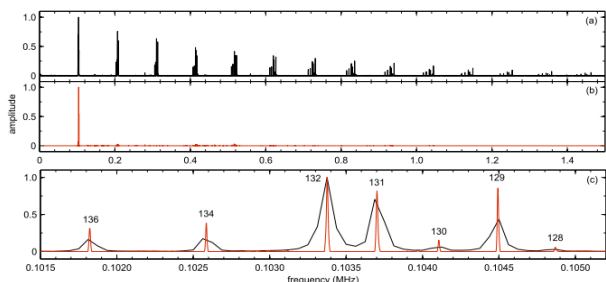


Figure 4 - Frequency analysis of  $Xe^+$  isotopes trapped for 8ms using (a) FFT with a Welch window and (b) comb-sampling with a window from 0.8 - 8 ms. Plot (c) shows the fundamental frequency from comb-sampling compared to the second harmonic of the FFT. The masses of the Xenon isotopes are indicated.

As a demonstration of the capability of the KEIRA-CHIMERA method, we have used it to separate the isobars  $N_2$  and CO.

With a mass difference of 0.011u, separation of these two molecules requires a mass resolution of greater than 2500. Figure 5 clearly shows two separate, well resolved, peaks for the isobars  $N_2$  and CO achieved from trapping the ions for 5 ms. The red vertical lines indicate the expected mass positions of the ions.

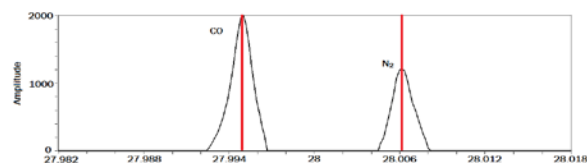


Figure 5 –  $N_2$  and CO peaks clearly resolved

### Conclusions

LEITs, such as KEIRA, have great potential as high resolution mass spectrometers. One fundamental problem, due to the non-sinusoidal nature of the time signal extracted from such devices, is that the commonly used method of Fourier analysis generated a large number of higher harmonics in the frequency spectrum. While these higher harmonics provided a high mass resolution the presence of so many made the generation of a complete mass spectrum non-trivial.

The use of the CHIMERA algorithm presented here uses data from multiple pick-ups to extract frequencies from LEITs with a high mass resolution at only the fundamental frequency. This enables the easy generation of a mass spectrum, realising the potential of LEIT’s as a powerful mass spectrometer.

### Acknowledgements

MJD and LB would like to acknowledge funding from the Department of Education and learning (NI). CRC acknowledges funding from EPSRC (Postdoctoral Research Fellowship at the Physical-Life Science Interface). OK and RBK acknowledge funding from the Leverhulme Trust.

### References

1. LH Anderson, O Heber and D. Zajfman, *J Phys. B: At. Mol. Opt. Phys.* **37**, R57 (2004)
2. J. D. Alexander et al., *Meas. Sci. Technol.* **21**, 045802 (2010)
3. O Kelly et al., *Central Laser Facility Annual Report: Femtosecond Pulse Physics*, 2008/2009.
4. JB Greenwood et al., *Rev. Sci. Inst.*, **82**, 043103 (2011)

# Fragmentation of Allene by Intense Femtosecond Lasers

Contact [j.greenwood@qub.ac.uk](mailto:j.greenwood@qub.ac.uk)

O Kelly, CR Calvert, RB King, MJ Duffy, L Belshaw,  
ID Williams and JB Greenwood

Centre for Plasma Physics,  
School of Mathematics and Physics,  
Queen's University Belfast

WA Bryan

Department of Physics, Swansea University

E Springate, CM Cacho, ICE Turcu

Central Laser Facility, STFC, Rutherford Appleton Laboratory

## Introduction

In the work presented here, fs-ionisation is coupled with a linear electrostatic trap to produce high resolution mass spectra of the small organic molecule, allene. The tuneability of femtosecond laser systems is exploited to look at the ionisation and fragmentation of allene in intense light with linear or circular polarisation. The success of these experiments will promote the applicability of fs lasers as a universal, reliable and tuneable ionisation source in mass spectrometry, both for chemical or trace analysis and structural analysis of complex systems.

Allene is a small organic molecule, consisting of three double bonded carbons in a linear alignment, with two pairs of hydrogens on either end ( $\text{H}_2\text{CCCH}_2$ ). The nature of the  $\pi$ -bonding between the carbons provides allene with a low ionisation potential (9.69 eV) while the appearance energy for ionisation and fragmentation e.g. for dehydrogenation is greater than 11 eV. The structure of allene is well understood theoretically [1] and so it is a good test case for the intense interactions in the present experiments.

## Experimental Technique

All experiments were performed with the KEIRA mass spectrometer with the Artemis Laser [2] at the Central Laser Facility. KEIRA has been described in detail elsewhere [3]. In brief, it is made of a series of apertured stainless steel electrodes that, with the application of kV potentials, forms an electrostatic cavity (as depicted in Figure 1) to enable ions to stably oscillate back and forth between the two electrostatic mirrors.

KEIRA is operated with a base pressure of  $10^{-9}$  mbar, increasing to  $10^{-7}$  mbar when allene gas is introduced to the cavity through a needle valve. The intense femtosecond laser is focussed onto this plume (see Figure 1), generating typically tens of thousands of ions per laser shot.

The spectrometer may be operated in two experimental modes: 1. Time of flight (ToF), where the second electrostatic region is reduced to zero such that the ions are not reflected, but are detected directly by a channel electron multiplier (CEM); or 2. Trapping mode, where the initial acceleration region is mirrored on the opposite side of the field free region. Two einzel lenses located either side of the field free region maintain the radial stability of the ions as they oscillate.

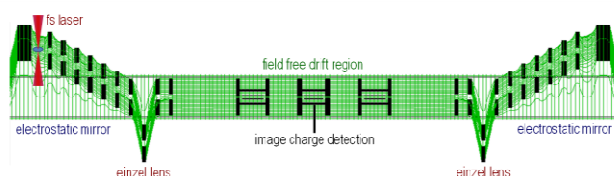


Figure 1: Potential energy surface of the KEIRA spectrometer.

Dimensions: 420 mm between the two maximum potential electrodes; field free drift region is 215 mm. [Adapted from the ion optics simulation software, Simion]

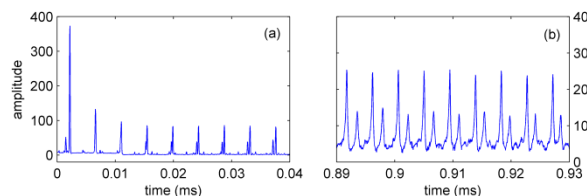


Figure 2: Typical trapping spectrum of allene, recorded using the central image charge detector in KEIRA. The allene gas was ionised in situ with 785 nm, 35 fs pulses of peak intensity  $4 \times 10^{14} \text{ Wcm}^{-2}$ , and summed over 10 000 shots. (a) 40  $\mu\text{s}$  window at the start of trapping. (b) 40  $\mu\text{s}$  window of the data after 0.9 ms of trapping.

Every time an ion species passes through one of the three pickup rings located in the field free region of the trap, their image charge is detected. In this way, periodic impulses for each trapped species are recorded (Figure 2), where the period is proportional to the square root of the ion's mass/charge. The initial peak shown clearly in Figure 2(a) has an amplitude of nearly 0.04 V per laser shot, which translates to 70 000 ions [4]. Through frequency analysis of this trapping spectrum using the CHIMERA algorithm [3], frequency information may be extracted and a high resolution mass spectrum is produced.

For the present experiments, 785 nm pulses with a duration of 35 fs were used. The repetition rate was set to 100 Hz to enable an ion trapping cycle of 10 ms. A 250 mm spherical Ag mirror was used to focus the light into the interaction region of the trap, providing a peak intensity of  $5 \times 10^{14} \text{ Wcm}^{-2}$  at the focus for 150  $\mu\text{J}$  pulses. The pulses were linearly polarised along the trap axis, and the polarisation could be changed to circular using a thin quarter wave plate.

## Results and Discussion

Figure 3(a) shows a mass spectrum of allene ionised by 35 fs linear polarized pulses, at an intensity of  $3.2 \times 10^{14} \text{ Wcm}^{-2}$ . This is a regime in which ionization is expected to result from tunnelling of an electron through the barrier induced by the laser's electric field. As well as the parent ion at a mass of 40, there are strong peaks corresponding to loss of H atoms along with doubly charged ions of these molecules. Breakage of a strong C=C double bond leading to  $\text{CH}_n^+$  and  $\text{C}_2\text{H}_n^+$  ( $n = 0-4$ ) fragments can also be seen. There are a number of possible mechanisms that could generate this molecular fragmentation.

The first relies on the fact that the molecule will have sufficient time, while still under influence of the field, to evolve into different conformations that allow access to dissociative pathways via resonant or virtual states, that are otherwise inaccessible when the molecule is in an equilibrium structure [5].

Alternatively, the strong laser field can modify the potential energy surface to produce field assisted dissociation [6]. For a stretched bond at a critical bond-length, the molecule has an increased probability of undergoing further ionisation (enhanced ionisation), or is further elongated until the bond breaks. Doubly charged ions formed by enhanced ionisation may also be

unstable, leading to Coulomb explosion to generate two singly charged fragments.

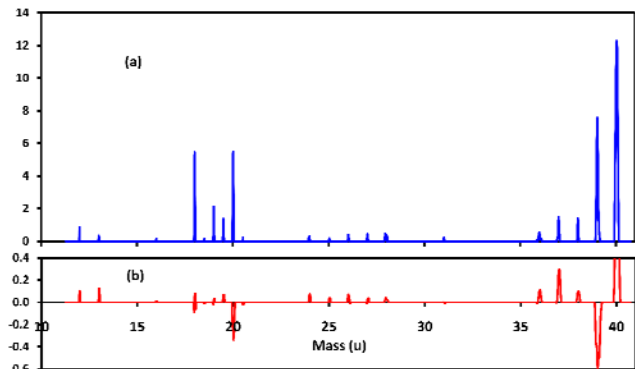


Figure 3: (a) mass spectrum of allene from interactions with 35 fs laser pulses with linear polarisation at an intensity of  $3.2 \times 10^{14} \text{ Wcm}^{-2}$ ; (b) the difference between linear and circular polarisation mass spectra.

Another mechanism is a consequence of the electron being under the influence of the field once it has tunnelled through the barrier. For a linearly polarised field, it is possible for the electron to change direction and be accelerated back to the core (re-scattering). Depending on the phase at which the electron is emitted, the returning electron can collide with the cation to induce secondary ionisation or fragmentation. Again, the doubly charged species may produce fragments by Coulomb explosion. Classically, the maximum kinetic energy with which the electron can return to the core with is  $3.17U_p$ , where  $U_p$  is the ponderomotive energy, which in this case is about 60 eV.

In contrast, for circularly polarised light, there is no rescattering as the electron is driven away from the core. Therefore a comparison between linear and circular results can reveal the influence of re-scattering. However, a straightforward comparison using the same intensity is not possible. To compare results for linear and circularly polarised pulses, the different cycle averaged rates for the two must be considered. If the ion yields as a function of the maximum electric field strengths for each polarisation condition are calculated using ADK tunnelling theory [7], the circular yields are higher as the electric field is always 'on' during a cycle. If the electric field strength for the circular polarisation is multiplied by a factor of 1.14, the two theoretical curves display excellent agreement in the saturation region. For experimental data, measurements taken at the same intensity have a maximum electric field strength which is  $\sqrt{2}$  lower for the circularly polarised pulses. Therefore, to compare the two mass spectra the circularly polarised experimental data should be taken at an intensity which is approximately a factor of  $(\sqrt{2}/1.14)^2 = 1.54$  higher than the linear [8].

Figure 3(b) displays the subtraction of a circularly polarized mass spectrum at an intensity of  $4.8 \times 10^{14} \text{ Wcm}^{-2}$  from the linearly polarized data ( $3.2 \times 10^{14} \text{ Wcm}^{-2}$ ) shown in figure 3(a). The relative amplitudes of the individual spectra have been normalised so that the contaminant water peak at 18 subtracts to zero, as this should be a good marker of the single electron tunnelling ionization yield.

It can be seen that the yield of all fragment ions is increased for linearly polarized pulses, with the exception of the peak at 39 corresponding to H loss for which there is a strong reduction. There are also more single charged (40) and slightly less doubly charged (20) parent ions produced.

This suggests that the circularly polarized pulses provide additional energy input to the molecule resulting in a boost in the other main peaks in the spectrum (20, 39), but with a reduced yield of the singly charged parent ion. These peaks are likely to be produced through resonant enhancement via the many excited states of the cation [5], so the fact that there are more photons in the

circularly polarized pulse and there will be differences in selection rules could explain this relative enhancement.

For all the other fragments, particularly those corresponding to multiple bond breakages which require substantial additional energy deposition (e.g.  $12 - \text{C}^+$ ,  $13 - \text{CH}^+$ ,  $24 - \text{C}_2^+$ ,  $36 - \text{C}_3^+$ ,  $37 - \text{C}_3\text{H}^+$ ), there is clear evidence that re-scattering is enhancing production of these fragments. For  $\text{CH}^+$  and  $\text{C}_2^+$ , the yields are increased by about a factor of 2 which in a re-scattering collision are probably caused by electron impact dissociative ionization of the cation.

## Conclusions

KEIRA has been successfully demonstrated as a high resolution mass spectrometer, suitable for studies of gas phase molecular species with intense femtosecond laser pulses. By changing the characteristics of the incident laser pulses, such as the polarisation, it is possible to extract information on the ultrafast dynamics that leads to bond breaking in small molecules. For allene we have found that when saturation intensities for single ionization are exceeded, there is an enhancement in the yield of fragment ions due to the re-scattering mechanism, especially for channels which correspond to more complete destruction of the molecule.

## Acknowledgements

O Kelly and RB King acknowledge funding from Leverhulme Trust. CR Calvert acknowledges funding from EPSRC (Postdoctoral Research Fellowship, at the Physics-Life Science interface). L Belshaw and M Duffy acknowledge funding from the Department of Employment and Learning (NI).

## References

1. MH Palmer 2006 *Chem. Phys.* **326** 631-640
2. ICE Turcu *et al* 2010 *Proc. SPIE* 746902
3. JB Greenwood *et al* 2011 *Rev. Sci. Instr.* **82** 043103
4. JD Alexander *et al* 2010 *Meas. Sci. Technol.* **21** 045802
5. AM Mebel, AD Bandrauk 2008 *J. Chem. Phys.* **129** 224311
6. S. Wang *et al* 2003 *J. Phys. Chem.* **107** 32
7. MV Ammosov *et al* 1986 *Zh. Eksp. Teor. Fiz.* **91** 2008
8. J Pedregosa-Gutierrez *et al* 2004 *Phys. Rev. Lett.* **93** 223001

# Beam-transport diffraction in near-infrared few-cycle strong-field experiments

Contact [w.a.bryan@swansea.ac.uk](mailto:w.a.bryan@swansea.ac.uk)

G. R. A. J. Nemeth and W A Bryan

Department of Physics, Swansea University, Swansea, SA2 8PP, UK and Central Laser Facility, Rutherford Appleton Laboratory, Harwell Science and Innovation Campus, Oxfordshire, OX11 0QX, UK

## Introduction

Ultrashort pulses of near-infrared (NIR) laser radiation have led to the production of attosecond pulses, either as pulse trains or in isolation. The generation of such coherent bursts of radiation requires an ultrabroadband laser oscillator producing sub-10 fs pulses, chirped pulse amplification to a peak power in excess of 1 GW and a self-referencing phase measurement allowing the relative phase of the carrier and envelope to be locked with respect to each other, referred to as carrier-envelope-phase (CEP) stabilization.

Modern titanium-sapphire oscillators and amplifiers generate near-transform-limited high power CEP-stable pulses with a duration of around 20 fs, which when focused into a Noble gas jet, initiates high harmonic generation (HHG) of XUV photons. This photon energy upconversion is the result of the strong-field initiating tunnel ionization of the Noble gas atom, propagation of the ejected electron in the time-varying field, followed by the release of additional odd-quanta of the fundamental photon energy as a single high energy photon upon recombination with the parent ion.

Focusing laser pulses with tens of femtoseconds duration into a gas jet will result in coherent XUV radiation released over a similar timescale, which if CEP-stabilized will result in a train of attosecond-duration pulses. Even if the drive laser is not CEP stable, by monochromating the XUV radiation through the use of multilayer mirrors or diffraction gratings can result in a highly useful source. However to access the attosecond regime, there must be one high-flux recombination event per NIR drive pulse. This can be achieved through optical gating techniques such as direct-optical gating as recently demonstrated. However the most common technique is to employ a CEP-stable few-cycle pulse (FCP): as the probability of tunnel ionization is highly nonlinear, there is only one half-cycle within the pulse that generates XUV radiation [1,2].

Compressing a transform-limited 20 fs pulse to a few cycles requires additional bandwidth, which may be produced by e.g. self-phase modulation (SPM) in a gas-filled hollow fibre [3]. This technique has been demonstrated in single-mode fibres for low peak power pulses, extended to the millijoule range through the use of hollow fibres and has potential to allow the spectral broadening of pulses of tens of millijoules when extended to planar or large volume waveguides. Dispersion control using prisms, gratings or multilayer chirped mirrors then allows the broadened pulse to be compressed. Here, we consider a hollow fibre with an internal bore of  $d = 250 \mu\text{m}$  such as would be employed to generate a few hundred microjoule FCP.

To couple the output of the Ti:sapphire laser system into the hollow fibre, transmission or reflection focusing is employed to optimally match the near-Gaussian profile of the laser with the  $\text{EH}_{11}$  mode of the fibre. The most efficient coupling is nominally achieved when the  $1/e^2$  diameter of the input beam is 0.65 times the fibre diameter. A static volume of gas can be employed to spectrally broaden pulses with an energy below 0.3 mJ; above this energy a pressure gradient [4] is advantageous

such that temporal and spatial distortions due to ionization and plasma processes at the input of the fibre are avoided. In either case, as the pulse propagates along the fibre, it is broadened by SPM and dispersed by the gaseous medium. If the fibre is too short, the broadening will be insufficient to generate a FCP; beyond an optimal length, broadening will render the pulse incompressible.

On the exit of the fibre, the termination of the waveguide and hard edge of the glass face cause a beam waist and diffraction. The output mode is a combination of modes but with optimum coupling will be predominantly the  $\text{EH}_{11}$  mode [1,2] which is a zeroth-order Bessel function of the first kind truncated at the first root, and  $a_1 = 125 \mu\text{m}$  is the radius of the hollow fibre.

Following propagation of around 1 m, the fibre output is recollimated on reflection from a spherical mirror, again introducing diffraction from the mirror edge. Temporal compression and beam transport into a vacuum chamber allows the diffraction from the fibre edge and recollimating mirror to dramatically alter the beam profile.

To facilitate the generation of an XUV attosecond pump and NIR femtosecond probe with variable delay, some form of material or spatial beamsplitting and filtering is required. We assume that at this point the NIR pulse is split with a thin glass beamsplitter, with one beam reflection focused into a gas-jet, and the resulting XUV separated from the NIR by metal filters then reflection focused into the interaction region of a spectrometer without encountering any material. It is the high cross-section for material absorption in the XUV that places this constraint on the optical system. To allow the XUV and other NIR pulse to be temporally and spatially overlapped requires the use of annular or segmented optics which will result in additional diffraction. Intensity control is also necessary in both NIR beams and again this must be achieved without additional material hence hard apertures are employed, further diffracting the beam.

In this work [5], we employ the Huygens-Fresnel diffraction equation to numerically model the influence of hard-edged optics on beam propagation in a typical attosecond beamline. The model incorporates a hollow fibre for spectral broadening, a hard-edged aperture for intensity control, and finite-diameter

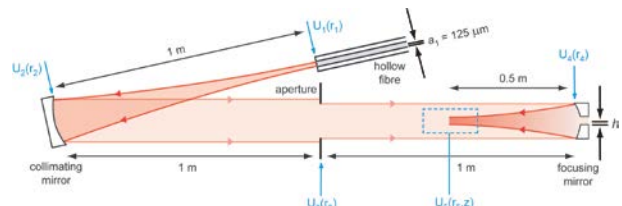


**Figure 1. Schematic of the optical system considered: a Bessel  $\text{EH}_{11}$  spatial mode propagates from the input plane at the exit of the hollow fibre via a spherical collimating mirror through an intensity-controlling aperture of variable radius  $a_3$ , and focused into the interaction region by a spherical mirror. The annulus is modified by increasing the radius  $h$  of the central hole from 0 to 2 mm.**

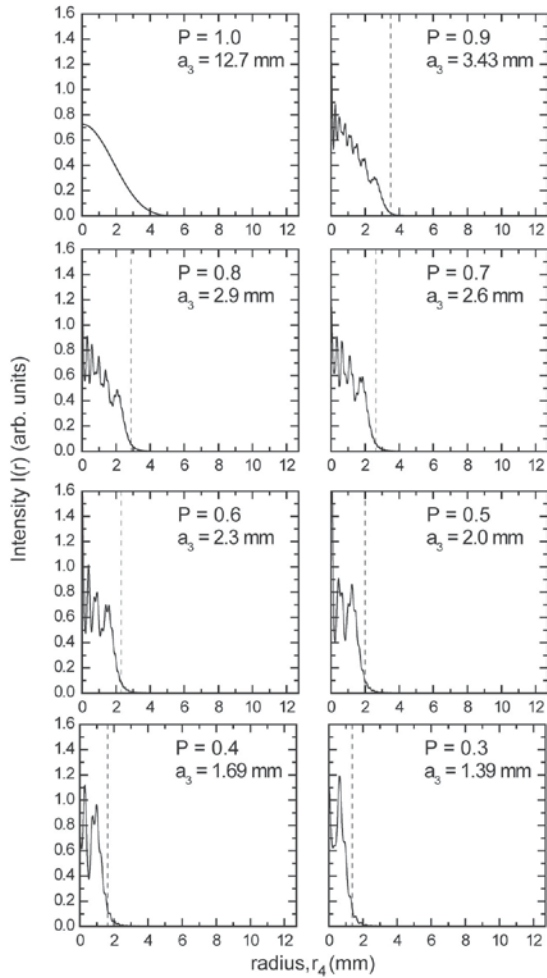


**Figure 2. Radial intensity distribution at the focusing mirror after propagating 1 m from the intensity-controlling aperture in the optical system illustrated in fig. 1. The aperture (radius  $a_3$ ) truncates the beam and reduces the relative power transmitted. The dotted line shows the position of the aperture edge.**

reflection focusing optics including annular optics, with application to strong-field and attosecond experimental science. Throughout, we assume a Gaussian mode has been coupled into the hollow fibre resulting in an  $\text{EH}_{11}$  Bessel output mode. This is then collimated by a finite diameter mirror, allowed to propagate through an aperture of varying diameter then reflection focused from a spherical mirror as illustrated in figure 1. We treat the case of an annular spherical mirror. It should be noted that we only consider the spatial characteristics of the diffraction process, taking no account for the broadband nature of the temporal pulse or nonlinear processes in the laser focus.

### Modelling and Results

As an example, consider the optical system illustrated in figure 1: The complex electric field at the collimating mirror is found by numerically evaluating the Huygen-Fresnel diffraction integral (HFDI) over the finite aperture of the fibre end. The imaginary component of the electric field contains phase information allowing the wavefront shape to be propagated. This process is then repeated for the collimating mirror which we define to have a radius of  $a_2 = 12.7$  mm, defining the integration limit of the HFDI. We define fully-open intensity-controlling aperture with  $a_3 = 12.7$  mm and focusing mirror with  $a_4 = 12.7$  mm. The limits  $a_2$ ,  $a_3$  and  $a_4$  are chosen to represent the hard edges imposed by 25.4 mm (1") diameter beamline optics typically used in experimental beamlines.

Figure 2 shows the effect of reducing the radius of the intensity-controlling aperture. Since the Airy disk contains 99.2% of the beam power, changes in the aperture size have little effect on the power transmitted for radii between 12.7 mm and 5.5 mm, though the low-intensity features present between these radii will be truncated and distorted. However, as the hard edge encroaches on the Airy disk, small changes in the transmitted power are immediately accompanied by dramatic changes in the transmitted beam profile. For an aperture radius,  $a_3 = 2.9$  mm, corresponding to a relative transmitted power,  $P = 0.8$  compared to  $a_3 = 12.7$  mm, the underlying Bessel profile is barely recognisable, dominated by multiple intensity peaks due to diffraction at the intensity-controlling aperture.

In Figure 3 we present the spatial intensity distribution and wavefront shape as a function of the optical power transmitted through the aperture onto an annular spherical focusing mirror. The annular mirror has an outer radius of  $a_4 = 12.7$  and a hole of radius  $h = 1$  mm. The integration limits of the HFDI are now  $h$  and  $a_4$ . As is apparent from figures 2 and 3, propagation from the fibre to the focusing mirror already introduces significant diffraction structure in the beam. A hole in the annular mirror introduces an additional hard edge and removes the highest-intensity section of the beam from the centre to the radius  $h$  of the Airy disk, causing additional diffraction effects as well as a reduction in the power transmitted to the focus. The maximum power in figure 3 corresponds to the aperture being the same diameter as the collimating mirror and the relative power transmitted by the aperture agrees with that shown in figure 4. As discussed earlier, this case is comparable to attosecond and XUV-NIR beamlines. Even at the highest power, there are obvious non-Gaussian features in the non-annular spherical mirror: cylindrically symmetric intensity lobes are generated on-axis and following the outer edge of the focal cone. As the power is decreased, the structure of the focal volume becomes more pronounced, with the 'V'-shaped distribution dominating. Again, a significant shifting of the peak spatial intensity is observed, to a greater extent than the non-annular case.

Figure 3 was produced from full three-dimensional plots of the focal volume, which require significant computing time to produce at sufficient accuracy to be meaningful. However, as can be seen from the figures, despite additional diffraction structure and spreading of the highest-intensity part of the focus, the peak intensity remains on axis. By solving the HFDI on axis, the peak intensity and focal shift can be quantified far more quickly and efficiently. Figure 4 has been produced using the on-axis intensity distribution only, at representative aperture radii  $a_3$ , where the step size in aperture radius is varied with peak power. These plots can be produced in timescales of tens of seconds, meaning this calculation is practicable for quantifying or verifying focal parameters during an experiment. The figure demonstrates how the peak spatial intensity and its location vary as a function of aperture radius for five spherical mirror hole radii from  $h = 0$  to 2 mm in 0.5 mm steps.

The spatial intensity depends on the distribution of power through the aperture and the diffractive influence of all other elements in the system. As a result, the peak intensity is heavily nonlinear with aperture radius. The local minimum around 7 mm is the result of a significant drop in peak intensity caused by the splitting of the peak into two separated by a few mm.

As apparent from figures 3 and 4 as the aperture is closed, the maximum spatial intensity is observed to translate along the  $z$ -axis by a measurable amount. This focal shift is quantified in figure 4 as a function of aperture radius and annular hole radius. For all hole radii, for an aperture radius above 4 mm, the focal shift is less than a millimetre. As the aperture is reduced below 4 mm, a dramatic shift of the focal position is predicted. With a hole radius of 2 mm and aperture radius of 3 mm (corresponding to a relative intensity of  $\sim 0.1$ ), a focal shift of 1

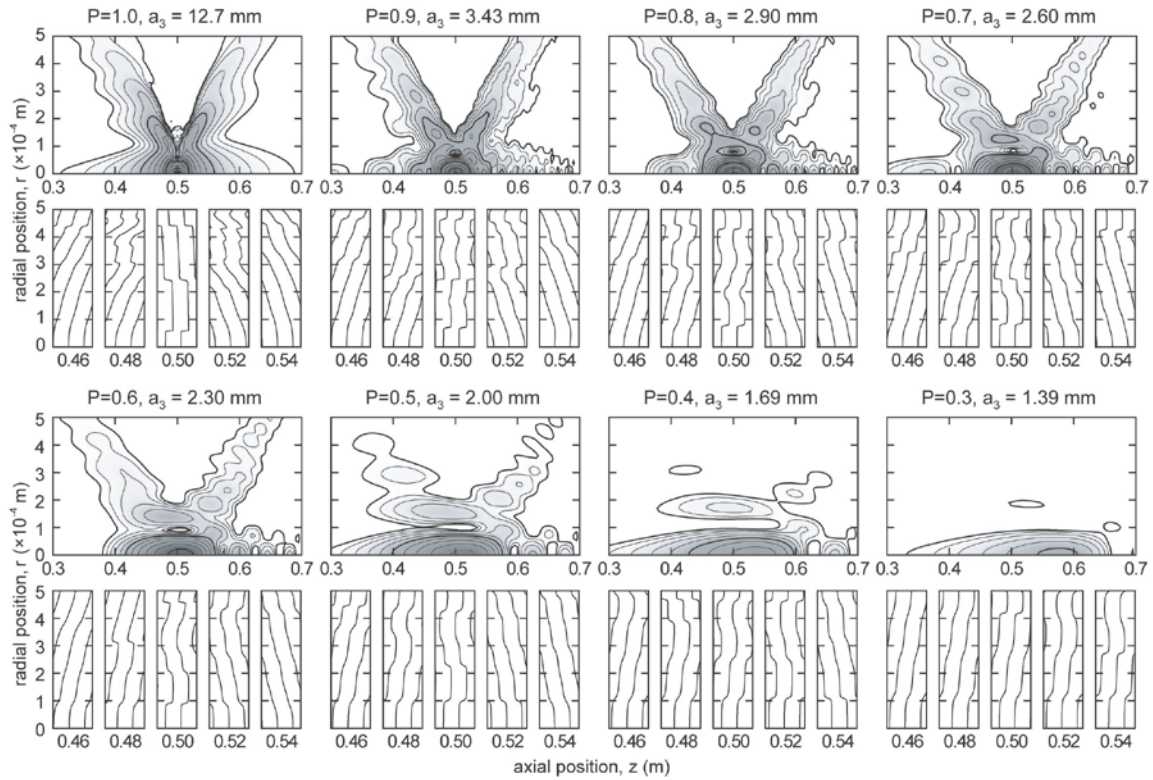


**Figure 3. Spatial intensity distribution and wavefront shape at the focus of the optical system in fig. 1 as a function of relative power,  $P$  transmitted by the aperture. Here the spherical focusing mirror has a circular hole at the centre of radius  $h = 1$  mm. The lowest relative intensity is  $10^{-3}$  and highest is  $10^0$ ; each thick contour represents an order of magnitude change, each fine contour is an intensity change of  $10^{0.2}$ . The power  $P = 1.0$  corresponds to the aperture radius being equal to the collimating mirror radius. Below each intensity plot the wavefront shapes are presented in  $2 \mu\text{m}$  slices; the wavefronts are separated by  $2\pi$ .**

cm is predicted. Such a shift could easily move the useful intensity region of the focal volume outside the source region of a spectrometer.

### Conclusions

Our numerical modelling of the focal volume using established methods applied specifically to a typical attosecond beamline, reveal significant changes to a focused beam when parameters are modified using typical non-dispersive methods, with clear

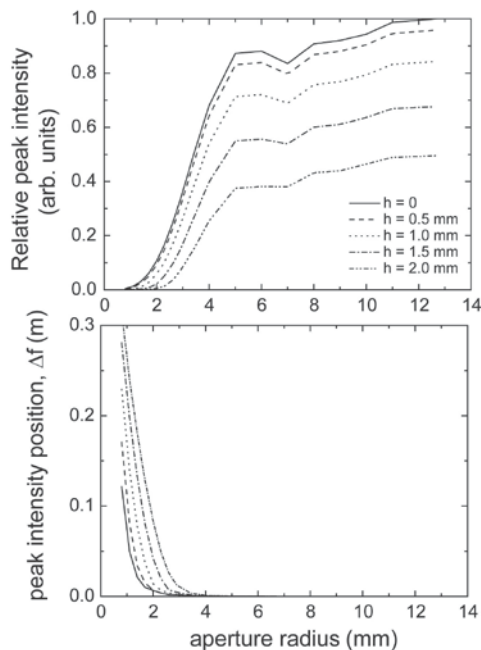


**Figure 4. Peak spatial intensity and position in the focal region as function of aperture radius relative to the peak intensity with the aperture fully open.**

implications to intensity- and spatially-resolved attosecond and few-cycle pulse experiments. The intensity structure in the focal region can become heavily structured and the peak intensity significantly offset from the geometric focus; these effects have been characterized for a range of conditions. Properly quantified, diffraction can be utilized advantageously to create regions of the focus where the intensity varies smoothly and phase variations are greatly reduced. Full three-dimensional focal volume modelling can be computationally intensive, but the on-axis intensity distribution can be computed quickly, revealing shifts in the focal position which are not predicted when geometric behaviour is assumed to be dominant. The method relies on a proper characterization of the input beam profile, since the beam propagation and therefore focal volume are strongly dependent on this. Our models can therefore be used to guide axisymmetric beamline design and construction, as well as optimisation of focal conditions in attosecond pulse production techniques and experiments.

### Acknowledgements

G. R. A. J. Nemeth acknowledges financial support from EPSRC and STFC.

### References

1. Brabec, T and Krausz, F. *Rev. Mod. Phys.* **72**, 545 (2000).
2. Krausz, F. and Ivanov, M. *Rev. Mod. Phys.* **81** 163 (2009)
3. Nisoli, M, de Silvestri, S, Svelto, O. *Appl. Phys. Lett.* **68**, 2793 (1996)
4. Robinson, J. S. *et al, Appl. Phys. B* **85**, 525 (2006)
5. Nemeth, G. R. A. J. and Bryan, W. A, *J. Mod. Optics* (accepted). DOI: 10.1080/09500340.2011.583073

# Dissecting charge and lattice order in 1T-TaS<sub>2</sub> with ultrafast XUV ARPES<sup>1</sup>

Contact [j.petersen1@physics.ox.ac.uk](mailto:j.petersen1@physics.ox.ac.uk)

**JC Petersen, A Cavalleri**

*Department of Physics, Oxford University, Clarendon Laboratory, Parks Road, Oxford  
Max Planck Group for Structural Dynamics, CFEL, University of Hamburg*

**S Kaiser, A Simoncig, HY Liu, AL Cavalieri**

*Max Planck Group for Structural Dynamics, CFEL, University of Hamburg*

**N Dean**

*Department of Physics, Oxford University, Clarendon Laboratory, Parks Road, Oxford*

## Introduction

Charge density waves (CDWs) underpin the electronic properties of many complex materials. The canonical source of CDW order is Fermi-surface nesting, driven by electron-phonon coupling via the Peierls mechanism [2]. In many systems there are also pronounced electron-electron correlations, and multiple orderings may coexist or compete. Characterizing the interplay between different interaction mechanisms, and the associated hierarchy of energy scales and time scales, is crucial to understanding CDW physics in real materials.

We use time- and angle-resolved photoemission spectroscopy with sub-30-fs XUV pulses to map the time- and momentum-dependent electronic structure of photoexcited 1T-TaS<sub>2</sub>, a two-dimensional Mott insulator with CDW ordering. Charge order, which splits occupied sub-bands at finite momentum, melts along with the Mott gap – both well before the lattice responds. This challenges the view of a CDW caused by electron-phonon coupling and Fermi-surface nesting alone, and suggests that electronic correlations originate charge order.

## 1T-TaS<sub>2</sub>

At room temperature 1T-TaS<sub>2</sub> is metallic, with a nearly commensurate charge density wave (CDW) [3]. Below 180 K the CDW becomes fully commensurate and locks into the lattice [4], generating a periodic lattice distortion (PLD), reducing the Brillouin zone, and back-folding the Ta-5d manifold. Gaps appear at the new band crossings, splitting off several Umklapp or ‘shadow’ bands [5]. A narrow band left at the Fermi level [6] is further split by Coulomb repulsion into two Hubbard bands separated by a Mott gap.

Excitation with an ultrashort laser pulse can promptly close the Fermi-level gap at the zone centre [7], but time-resolved electron diffraction [8] shows that long-range structural order does not completely relax. Meanwhile, time resolved core level photoemission measurements suggest that the onsite charge density is already perturbed within 100 fs [9], implying that charge and lattice order may decouple at early times.

## Methods

Our measurements employ the time-resolved laser ARPES system at Artemis in the Central Laser Facility [10]. A 1-kHz beam of 30-fs amplified laser pulses is split in two. One beam stimulates the sample; the other generates harmonics in argon, in a vacuum beamline. A 20.4 eV harmonic, selected by a grating monochromator, is focused onto the sample in a UHV chamber. Photoelectrons emitted after each XUV pulse are collected and analyzed, revealing the distribution of electrons in

**C Cacho, ICE Turcu, E Springate**

*Central Laser Facility, STFC Rutherford Appleton Laboratory*

**F Frassetto, L Poletto**

*LUXOR, CNR-INFN, Padova, Italy*

**S Dhesi**

*Diamond Light Source Ltd.*

**H Berger**

*Institute of Physics of Complex Matter, EPFL, Lausanne, Switzerland*

the sample as a function of energy and momentum. We vary the delay between 790-nm and XUV pulses to follow the time evolution of electronic structure through the photoinduced insulator-to-metal transition.

## Results

The first panel of Fig. 1 shows a photoemission intensity map of band structure in the low-temperature phase. Reduced intensity at the Fermi level,  $E_f$ , indicates the opening of the Mott gap above the lower Hubbard band (LHB). A CDW gap between sub-bands is seen at the reduced Brillouin zone boundary (the M point). High-momentum states folded back into the first zone reappear at  $k=0$  (the  $\Gamma$  point).

After photostimulation by a laser pulse, the Mott and CDW gaps both collapse within a few tens of fs, shown in subsequent panels. These spectral changes are highlighted in the energy distribution curves of Fig. 2. At  $\Gamma$  there is a rapid loss of intensity in the LHB, and a filling in of states at and above  $E_f$ , both associated with Mott-gap collapse. At M, the sub-band splitting is lost as the distinct peaks merge into a single feature.

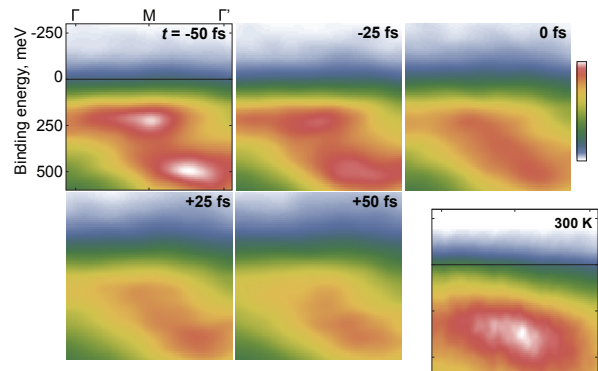


Fig. 1: Photoemission intensity as a function of electron momentum and energy, at 14 K, during the process of CDW melting. Immediately upon photostimulation, the band structure approximates that seen at room temperature (bottom right panel).

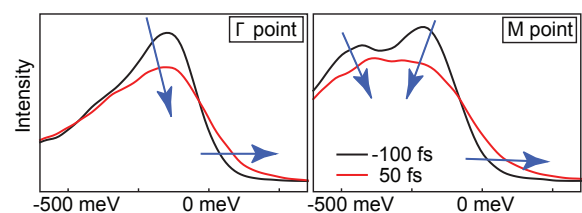


Fig. 2: Energy distribution curves showing collapse of the Mott (left) and CDW (right) gaps.

Not all changes to the electronic structure proceed so promptly. Figure 3 shows a more detailed examination of the time-dependence at  $\Gamma$ . At the Fermi level, where the increase in intensity corresponds to the collapse of the Mott gap, the transition is faster than the 30-fs resolution of the experiment. In contrast, at the lower energies of the uppermost Umklapp band (U1) at  $\Gamma$  the response is slower, well described by a transient response with a timescale of a half-cycle of the amplitude mode. This is consistent with a reduction in spectral weight brought about by relaxation of the PLD, which proceeds on structural rather than electronic time scales [8].

To illustrate this idea further, Fig. 4 shows the changes in intensity across the entire momentum range. The first panel shows relative changes from -50 to +50 fs relative to the arrival of the pump pulse; the second panel shows changes between +50 and +200 fs. The immediate response involves a loss of intensity in each band, but particularly at the peak of the LHB, and a gain in intensity at the Fermi level and above as the Mott state melts and hot electrons are created. In the delayed response, intensity is lost in U1 at  $\Gamma$  and reappears across the reconstructed zone boundary. This provides a direct snapshot of the unfolding of the Brillouin zone. Overall intensity is lost below the LHB peak and gained above it, as the PLD begins to relax and the band edge moves upward.

### Discussion

The fact that these different processes take place on distinctly electronic and structural timescales gives new information about both the static band structure of 2D CDW materials, and the process by which they melt after ultrafast excitation. To explain the rapid closing of the zone-boundary gap we must conclude that the CDW order is lost on sub-vibrational timescales, and that the zone-boundary gaps reflect the broken symmetry of charge density in the CDW ground state. On the other hand, the intensity of the shadow bands at the zone centre must be a manifestation of the PLD. Thus the CDW melts via prompt destruction of the charge order, to which the lattice then responds on its own timescale.

### Conclusions

Time-resolved ARPES with XUV radiation allows us to study the relaxation of a charge density wave in photo-stimulated 1T-TaS<sub>2</sub>, measuring charge order at the edge of the reconstructed Brillouin zone with sub-vibrational time resolution. By clocking the evolution of various changes, we assign specific features of the electronic structure to individual aspects of the ordered ground state. The gaps in the zone-boundary spectral function originate from the charge density ordering, which melts promptly after photostimulation. Subsequently, spectral intensity migrates from shadow bands in the first zone back out to higher momentum, revealing the unfolding of the BZ that accompanies incipient lattice relaxation along the coordinate of the Raman active amplitude mode following photo-doping [8].

This hierarchy of time scales indicates that charge and lattice order must decouple at early times, so that it will clearly be necessary to go beyond the phase- and amplitude-mode picture of CDW dynamics [2] to understand this system. An electronic origin for the Umklapp gaps also casts into doubt the dominant conception of the thermal phase transition, as being primarily driven by nesting with Mott physics following. Instead, electronic correlations seem to play a much more central part in CDW ordering itself.

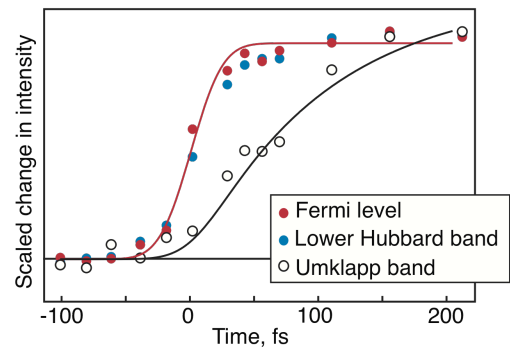


Fig. 3: Time evolution of photoemission intensity for key spectral features: Gain at the Fermi level, loss in the LHB, and loss in U1 at the zone centre. Red curve: instrumental response. Black curve: expected transient response with a timescale of half an amplitude-mode cycle [1].

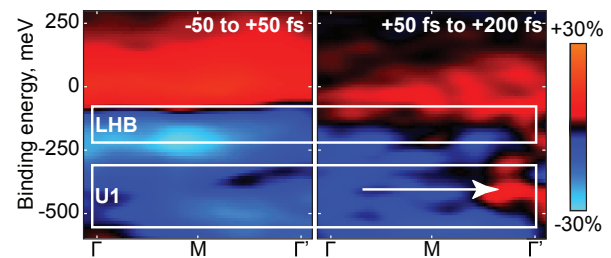


Fig. 4: Differential maps showing prompt and delayed changes in photoemission intensity.

### References

1. JC Petersen et al. *Phys. Rev. Lett.*, in press (2011); arXiv:1010.5027
2. G Grüner. *Density Waves in Solids*. Perseus (2004)
3. JA Wilson, FJ DiSalvo and S Mahajan. *Adv. Phys.* **24** 117 (1975); P Fazekas and E Tosatti. *Phil. Mag. B* **39** 229 (1979)
4. B Sipoš et al. *Nature Materials* **7** 960 (2008)
5. L Perfetti et al. *Phys. Rev. B* **71** 153101 (2005)
6. K Rossnagel and NV Smith. *Phys. Rev. B* **73** 073106 (2006)
7. L Perfetti et al. *Phys. Rev. Lett.* **97** 067402 (2006)
8. M Eichberger et al. *Science* **468** 799 (2010)
9. S Hellmann et al. *Phys. Rev. Lett.* **105** 187401 (2010); K Ishizaka et al. *Phys. Rev. B* **83** 081104(R) (2011)
10. E Turcu et al. *Proc. SPIE* **7469** 746902 (2010)

# Double slit interferometry to measure the EUV refractive indices of solids using high harmonics

Contact law504@york.ac.uk

L. A. Wilson, A. K. Rossall, E. Wagenaars, G. J. Tallents

The Department of Physics, The University of York  
York, YO10 5DD, UK

## Introduction

Accurate values of the optical properties of materials are required to make extreme ultraviolet (EUV) optics such as multilayer mirrors which are required for lithography, EUV astronomy and plasma diagnostics<sup>1</sup>. The properties of aluminium as considered in this report are particularly important as it is frequently used as a filter material and is an ideal material for theoretical comparison<sup>2</sup>.

The refractive index  $n(\omega)$  of a material is dependent on the photon energy and both real and imaginary components vary rapidly around absorption edges<sup>1</sup>. The complex refractive index is given by:

$$n(\omega) = 1 - \frac{n_a r_e \lambda^2}{2\pi} (f_1^0(\omega) - i f_2^0(\omega)) = 1 - \delta(\omega) + i\beta(\omega)$$

where  $n_a$  is the atomic density,  $r_e$  is the classical electron radius,  $\lambda$  is the wavelength,  $f_1$  and  $f_2$  are the real and imaginary parts of the scattering factor<sup>3</sup>. The real part  $\delta(\omega)$  determines the dispersion and the phase shift of electromagnetic radiation within a material, while the imaginary part  $\beta(\omega)$  is related to its opacity. At EUV wavelengths almost all solid materials are opaque with attenuation lengths  $< 1\mu\text{m}$ , so the imaginary refractive index component is significant.

The real and imaginary parts of the refractive index can be related by the Kramers - Kronig relationship allowing the real part of the refractive index to be determined indirectly from measurements of the absorption over a large range of the spectrum<sup>4,5,6</sup>. Both real and imaginary components for aluminium between 77.0 nm and 113.5 nm (11 eV - 16 eV) have been previously calculated from the Fresnel coefficients derived from measurements of reflectance as a function of angle of incidence<sup>7,8</sup>. Independent measurements of  $\delta(\omega)$  for aluminium and nickel from 60 eV - 80 eV, and silicon and ruthenium from 89 eV - 105 eV have also previously been undertaken using interferometry methods which allow simultaneous measurements of  $\delta(\omega)$  and  $\beta(\omega)$ , with the coherent EUV radiation provided by undulator beamlines<sup>3,9</sup>.

Measurements of the transmission of aluminium have been made using Ne-like Ge and Ni EUV lasers at 63.3 eV and 53.7 eV<sup>10</sup> and between the plasma frequency at 15 eV and the L<sub>3</sub> edge at 72.7 eV<sup>11</sup> using EUV emission from a laser produced plasma.

There are uncertainties in EUV refractive indices, especially where values change rapidly near absorption edges and in materials, in particular aluminium, which have oxide layers<sup>10,11</sup>. Examples of discrepancies between data sets for Al can be seen in figure 3, which compares measured photo absorption data with calculated data from Henke et al<sup>4</sup>, the CXRO database<sup>12</sup> and Shiles et al<sup>5</sup>.

Refractive indices of materials heated so that ionisation occurs are not well known. Values of opacities in the EUV region, at high to moderate energy densities rely on large theoretical codes which require benchmarking with experimental data. The opacities of materials under high temperature and density conditions have applications in both astrophysics and ICF. The opacity of iron is of particular importance in modelling solar structure. There is a potential for further work using the method outlined in the report for measuring the optical properties of laser heated materials.

C. Cacho, E Springate, E. Turcu

Central Laser Facility, STFC Rutherford Appleton Laboratory  
Didcot, Oxon, OX11 0QX, UK

## Double Slit interferometry

Odd harmonics between 17eV and 42eV were generated with an 800nm laser wavelength focused to an intensity of around  $10^{14} \text{ Wcm}^{-2}$  in an argon gas jet on the Artemis Facility at the Rutherford Appleton laboratories. A monochromator allowed the selection of individual harmonics. The divergence of the beam is estimated to be 1mrad with a repetition rate of 1 kHz and a 35fs pulse length. The average peak flux of the 17th harmonic was measured to be  $1.1 \times 10^{10}$  photons/s.

The range of different harmonics allowed simultaneous measurements of the real and imaginary parts of the refractive index as a function of photon energy for harmonics from 11 to 25 (17 eV - 39 eV) using a double slit interferometry method. Pairs of slits of 15 $\mu\text{m}$  width and 50 $\mu\text{m}$  separation were used. One half of one of the slits was covered in a layer of the sample material. This sample layer results in a fringe shift and a change in fringe visibility of the interference fringes relative to the interference pattern from the uncovered part of the slit which could then be used as a reference. Measurements were made for samples of Al and Fe.

This double slit interferometry method can also be used to measure the spatial coherence of the Artemis harmonic beam from a measurement of the fringe visibility ( $V$ ) as a function of slit separation<sup>13</sup>. For an uncovered pair of equally illuminated slits the fringe visibility is equal to the magnitude of the complex coherence factor ( $\gamma$ ).

All the slits were placed 10cm from the monochromator exit slit and the interference patterns were detected on a multi-channel plate (MCP) detector positioned 120cm from the slits the output of which was then imaged on to a CCD camera. In order to reduce the signal to noise ratio, data was taken with 937ms exposure for a series of 50 images with the same target. The repetition rate of the beam was 1 KHz giving a total of 46850 shots per target. These images were then summed to give a final image of the interference pattern.

To measure the complex coherence factor ( $\gamma$ ) of the harmonic beam, pairs of blank slits of 25 $\mu\text{m}$  separation 15 $\mu\text{m}$  width, 50 $\mu\text{m}$  separation 15 $\mu\text{m}$  width and 75 $\mu\text{m}$  separation 10 $\mu\text{m}$  width were used. This was measured for harmonics 11 - 29. This could then also be used to determine the transmission ( $T$ ) through a covered slit from a measurement of the fringe visibility ( $V$ ) given by:

$$V = \frac{2\sqrt{T}}{1+T} |\gamma|$$

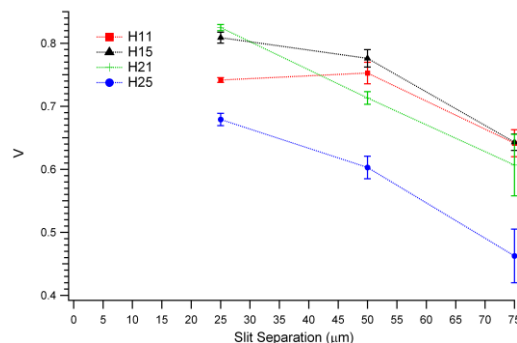


Figure 1: Harmonic coherence as a function of slit separation.

The fringe visibility as a function of slit separation for harmonics 11, 15, 21 and 25 are shown in figure 1. There is a high coherence of between 70% - 80% for the majority of harmonics up to the separation of 50 $\mu$ m used to measure the refractive indices. Coherence tended to decrease above harmonic 21. The accuracy of this method is dependent on the equal illumination of the slits; unequal intensity will result in a decrease of fringe visibility and an underestimate of the coherence. The slits were positioned in the beam to maximise the peak intensity and visibility of fringes. An estimate of the effect of a ratio of intensities of 0.70 through each slit, only gives a decrease in visibility of  $\leq 2\%$ .

In order to reduce errors in the measurement of the refractive index and to reduce the effect aluminium oxide, several different thicknesses of the sample foil were used. For aluminium sample thicknesses were measured to be  $93 \pm 1$  nm,  $585 \pm 3$  nm,  $610 \pm 5$  nm and  $800 \pm 2$  nm. The iron Samples had thicknesses of  $29 \pm 1$  nm,  $43 \pm 1$  nm,  $62 \pm 2$  nm.

## Results

Phase shifts were measured from fringe shifts for each aluminium sample from harmonics 11 to 25. Data for the thickest foil (800nm) was only used for harmonics 19 and 23 due to the very low fringe visibility in this photon energy range. Figure 2 shows the measured values (crosses) compared to experimental results from by Larruquert et al<sup>7,8</sup>, the CXRO database<sup>12</sup> (dashed line) and tabulated data taken from Smith et al<sup>6</sup> and Shiles et al<sup>5</sup>. Generally our measured values are lower than given in Shiles et al, showing increasing discrepancies at lower photon energies. The errors shown in the phase shift are derived from the deviation between repeated results, for harmonics 11 to 21 and thicknesses of 93nm and 585nm, and the error in measurements of fringe position. For some images there is a tilt in the fringes along the sample covered region. This was corrected using a measurement of the tilt angle which allowed using a measurement of the extra shift to the fringes. The origin of this tilt is still being investigated and may reflect a slow change in the phase of the harmonic along the slit.

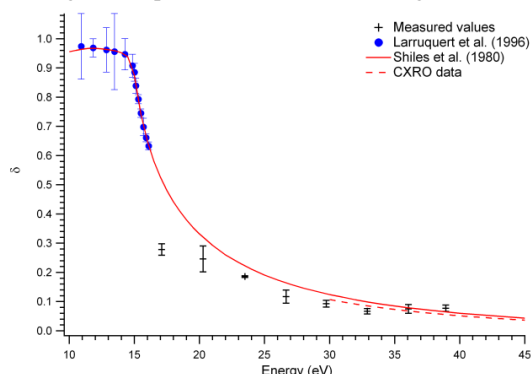


**Figure 2:** Measurements of the real component of the refractive index of Al compared to the CXRO database, Shiles et al and previous experimental work by Larruquert et al.

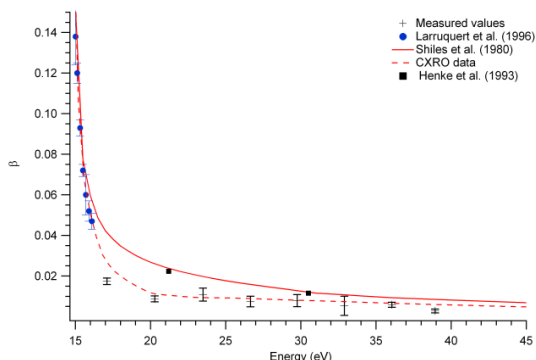


**Figure 3:** Measurements of the imaginary component of the refractive index of Al compared to the CXRO database, Henke et al, Shiles et al and previous experimental work by Larruquert et al.

Fringe visibility measurements were made for harmonics 11 to 25, for the 3 thinnest aluminium foils and for all iron foils. Figures 3 and 4 show the measured data. Comparisons to published data sets are also shown. For Al this data generally shows good agreement with the CXRO data with values lower than expected from the Henke et al<sup>4</sup> and Shiles et al<sup>5</sup> data in particular at lower energies. There are some deviations at 17 eV and 39 eV with the CXRO data. The iron delta data shows higher values of beta compared to both Henke et al and CXRO data, again the largest deviations appear at 17eV and 39eV. The errors shown in the figures arise from both the spread of repeated results, as for Al delta, and from the measurement of the fringe visibility.

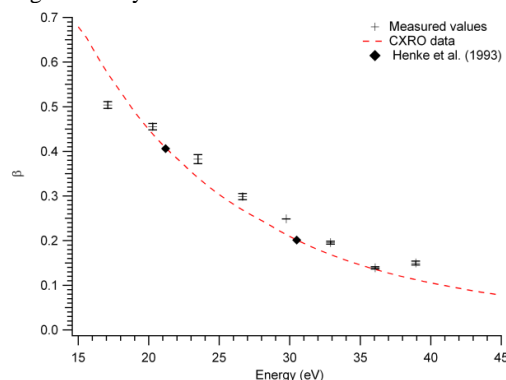


**Figure 4:** Measurements of the imaginary component of the refractive index of Fe compared to the CXRO database and previous experimental work by Larruquert et al.

## Conclusions

The coherence of the Artemis harmonic beam has been measured to be between 70 – 80% up to harmonic 21 over at least 50 $\mu$ m beam width. Measurements of the real ( $\delta$ ) and imaginary ( $\beta$ ) parts of the refractive index of aluminium and the imaginary part of iron have been measured from 17eV – 39eV. Aluminium beta values show good agreement with CXRO database values. Iron beta measurements show some deviation from the CXRO and Henke et al. data, generally showing higher values of beta. Al delta values also show discrepancies at low values of photon energy.

## References

- <sup>1</sup> D. Attwood, *Soft X-rays and Extreme Ultraviolet Radiation*, (Cambridge University Press, 1999)
- <sup>2</sup> B Nagler et al, *Nature Physics* **5**, 693 (2009).
- <sup>3</sup> K. Rosfjord et al, *Proc. of SPIE*, **5538**, 92 (2004)
- <sup>4</sup> B. Henke, E. M. Gullikson, J. C. Davis, *Atomic Data and Nuclear Tables*, **54**, 181 (1993)
- <sup>5</sup> E. Shiles et al, *Phys. Rev. B* **22**, 1612 (1980)
- <sup>6</sup> D. Y. Smith, E. Shiles, M. Inokuti, *Handbook of optical constants of solids*, edited by E. D. Palik, part II.1 p. 369 (Academic press, 1985)
- <sup>7</sup> J. I. Larruquert, J. A. Méndez, J. A. Aznárez. *Appl. Opt.* **35**, 5693 (1996)
- <sup>8</sup> J. I. Larruquert, J. A. Méndez, J. A. Aznárez. *Appl. Opt.* **34**, 4893 (1995)
- <sup>9</sup> C. Chang et al, *Opt. Lett.* **23**, 1028 (2002).
- <sup>10</sup> R. Keenan et al, *J. Phys. B.* **35** : L447 (2002)
- <sup>11</sup> E. M Gullikson et al. *Phys. Rev. B.* **49**, (16) 283 (1994)
- <sup>12</sup> Center for X-ray optics, Lawrence Berkeley National Laboratory, [http://henke.lbl.gov/optical\\_constants/](http://henke.lbl.gov/optical_constants/)
- <sup>13</sup> T. Ditmire et al. *Phys. Rev. Lett.* **77**, 4756 (1996)

## Probing the microscopic origin of laser-induced ultrafast spin dynamics using time resolved photoemission/MOKE

Mark Willcox<sup>1</sup>, Cong Lu<sup>1</sup>, Tuyuan Cheng<sup>1</sup>, Jing Wu<sup>1</sup>, Yongbing Xu<sup>1</sup>, Elaine Seddon<sup>2</sup>, Cephise Cacho<sup>3</sup>, Edmond Turcu<sup>3</sup>, Emma Springate<sup>3</sup>.

1, Physics/Electronics Department, University of York, York, YO10 5DD;

2. Photon Science Institute, University of Manchester;

3. The Artemis Station, CLF, RAL.

One of the most intriguing issues in today's nanomagnetism is the dynamics of spin systems at down to femtosecond timescales - **femtosecond magnetism**. Interest in this challenging field is fuelled both by the desire to develop novel concepts for ultrafast switching of spintronic devices and by the scientific need to establish fundamental understanding of spin systems in extreme non-equilibrium cases. Beaupaire and his co-workers reported their pioneering work on ultrafast magnetisation dynamics, induced by femtosecond laser pulses, in ferromagnetic transition metals in 1996 [i]. They observed that the time-resolved magneto-optical contrast dropped by 50% on a timescale of 1-2 ps following the absorption of a 60 fs laser pulse. This rapid reduction was interpreted as non-equilibrium heating of the spins, electrons, and the lattice, resulting in an ultrafast demagnetisation of the sample. The non-equilibrium states developed in magnetic materials following intense fs laser excitation represent a subject that has been widely investigated over the last decade [ii].

This paper reports the experimental results from our first beam time at the STFC's Artemis beam line on combined time resolved photoemission spectroscopy and time-resolved magneto optical Kerr effect (TR-MOKE) measurements. Our aim is to explore the microscopic mechanisms of ultrafast demagnetisation by mapping time-resolved energy band structures at the same time as monitoring time-resolved global magnetisation with femtosecond temporal resolution after ultra short pulse laser excitation in ferromagnetic iron thin films - which are grown *in-situ*.

The growth system, assembled during the beam time, operated well and the single crystal Fe thin-films were grown. MOKE loops obtained *ex-situ*, Fig. 1, show the characteristic magnetic uniaxial anisotropy of the epitaxial Fe/GaAs(100) system with the easy axis along the [011] direction and hard axis along the [0-11] direction. The zero time-delay between the XUV probe pulse and the 800nm pump pulse was precisely located by time-resolved MOKE using the zero-order light of XUV as the probe. Clear time-dependent MOKE and reflectivity signals were obtained at various laser fluences for determining the relationship between the dynamic magnetic reversal and the electronic structure as shown in the Fig 2. An ultrafast rise in the reflectivity shows the electron temperature reaches its maximum around 200fs after laser excitation. This leads to a demagnetisation maximum about 100 fs later the peak electron temperature.

Time-resolved photoemission spectroscopy was also performed. The spatial overlap of the pump and the probe beams was checked on the sample using a CCD camera to visualise the zero order light spot and the pump spot. The XUV spot position is well defined by looking at the zero order light on the beamline. Even though the expected large MLD was not observed, possibly due to an undesirable level of oxidation at the sample surface, the experimental measurements have been logically carried out and the data has been thoroughly analysed. Additionally, space charge effects of both the pump and probe at different powers were observed.

Figure 1. Magnetisation loops from an Fe(56ML)/GaAs(100) sample grown in-situ in Artemis—and measured in York using the MOKE technique. The loops show characteristic magnetic uniaxial anisotropy, which is characteristic of a single crystal Fe thin film on GaAs(100).

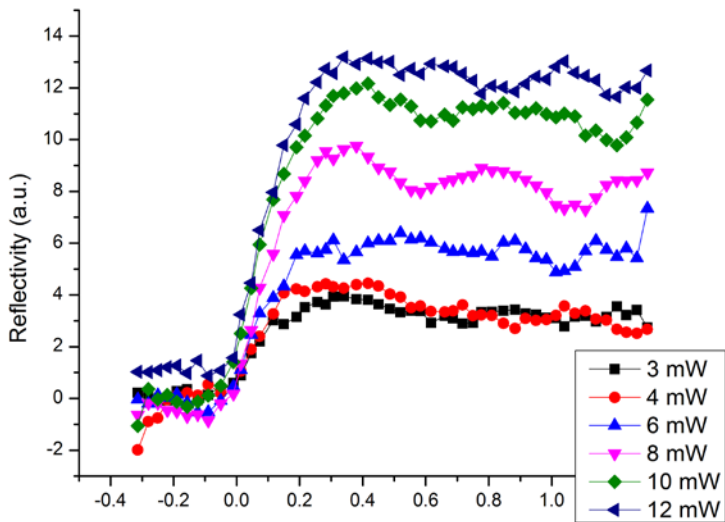
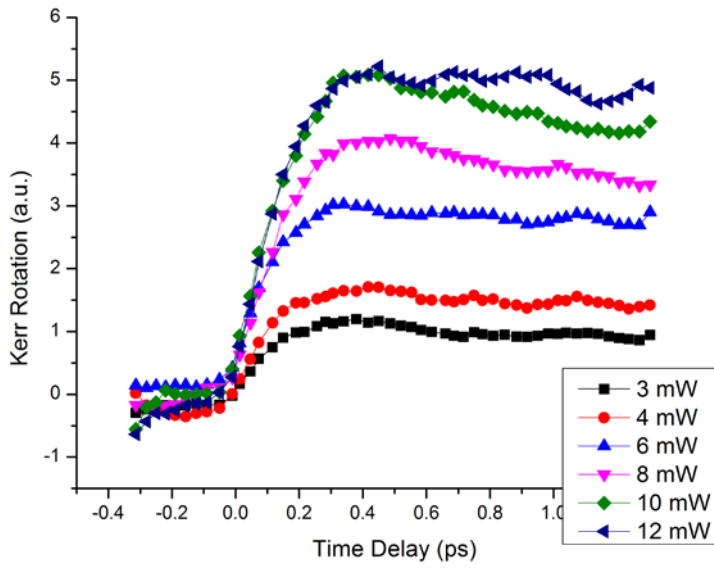
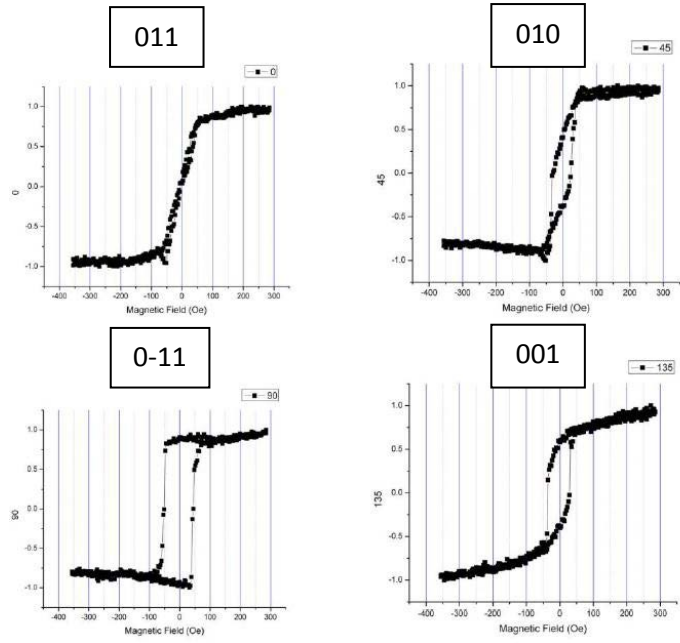


Figure 2. Kerr rotation and reflectivity versus time delay between probe and pump. - Observed from a 56 ML Fe on GaAs sample. Right: Peak signals versus pump power for the same thin film.

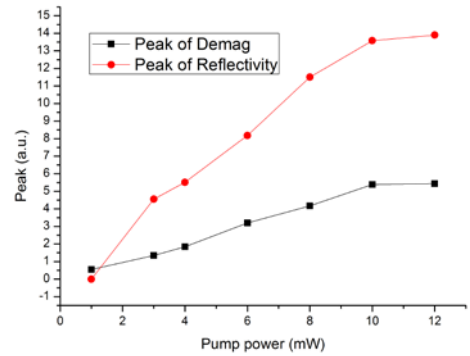
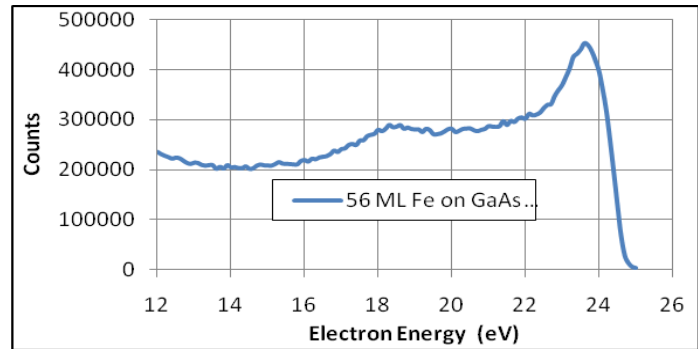


Figure 3. A raw photoemission spectrum obtained from a 56 ML Fe film on GaAs (100). The right-most peak is the Fe 3d electron peak. The oxidation is visible at 18.2 eV.



- 
- i E. Beaurepaire, J. C. Merle, A. Daunois, J. Y. Bigot, *Phys. Rev. Lett.* **76**, 4250 (1996).  
 ii B. Koopmans, M. V. Kampen, J. T. Kohlhepp and W. J. M. de Jonge, *Phys. Rev. Lett.* **85** 844 (2000). T. Kampfrath, R. G. Ulbrich, F. Leuenberger, M. Munzenberg, B. Sass, and W. Felsch, *Phys. Rev. B* **65**, 104429 (2002). J. Y. Bigot, L. Guidoni, E. Beaurepaire, and P. N. Saeta, *Phys. Rev. Lett.* **93** 077401-1, (2004). R. Gomez-Abal, O. Ney, and K. Satitkovitchai, *Phys. Rev. Lett.* **92**, 227402-1, (2004). G. P. Ju, et al, *Phys. Rev. Lett.* **94**, 087202, (2005). . Wilks, R. J. Hicken, M. Ali, and B. J. Hickey, *J. Appl. Phys.* **97**, 10A705, (2005). C.D. Stanciu, F. Hansteen, A. V. Kimel, A. Tsukamoto, A. Itoh, and Th. Rasing, *Phys. Rev. Lett.* **99**, 047601 (2007); C. Bunce, J Wu, G Ju, B Lu, D Hinzke, N. Kazantseva, U. Nowak, and R. Chantrell, *Phys. Rev. B* **81**, 174428 (2010).